

NAVAL POSTGRADUATE SCHOOL

Monterey, California



THESIS

A NUMERICAL STUDY OF FUEL-OPTIMAL LOW-EARTH-ORBIT MAINTENANCE

by

Lawrence E. Halbach

December 2000

Thesis Advisor:
Thesis Co-Advisor:

I. M. Ross
Fariba Fahroo

Approved for public release; distribution is unlimited.

REPORT DOCUMENTATION PAGE

Form Approved
OMB No. 0704-0188

Public reporting burden for this collection of information is estimated to average 1 hour per response, including the time for reviewing instruction, searching existing data sources, gathering and maintaining the data needed, and completing and reviewing the collection of information. Send comments regarding this burden estimate or any other aspect of this collection of information, including suggestions for reducing this burden, to Washington headquarters Services, Directorate for Information Operations and Reports, 1215 Jefferson Davis Highway, Suite 1204, Arlington, VA 22202-4302, and to the Office of Management and Budget, Paperwork Reduction Project (0704-0188) Washington DC 20503.

1. AGENCY USE ONLY (Leave blank)		2. REPORT DATE December 2000	3. REPORT TYPE AND DATES COVERED Master's Thesis
4. TITLE AND SUBTITLE A Numerical Study of Fuel-Optimal Low-Earth-Orbit Maintenance			5. FUNDING NUMBERS
6. AUTHOR(S) Halbach, Lawrence E.			
7. PERFORMING ORGANIZATION NAME(S) AND ADDRESS(ES) Naval Postgraduate School Monterey, CA 93943-5000			8. PERFORMING ORGANIZATION REPORT NUMBER
9. SPONSORING / MONITORING AGENCY NAME(S) AND ADDRESS(ES)			10. SPONSORING/MONITORING AGENCY REPORT NUMBER
11. SUPPLEMENTARY NOTES The views expressed in this thesis are those of the author and do not reflect the official policy or position of the Department of Defense or the U.S. Government.			
12a. DISTRIBUTION / AVAILABILITY STATEMENT Approved for public release; distribution is unlimited.			12b. DISTRIBUTION CODE
13. ABSTRACT (maximum 200 words) <p>This thesis studies the fuel optimal periodic reboost profile required to maintain a spacecraft experiencing drag in low-earth-orbit (LEO). Recent advances in computational optimal control theory are employed, along with a Legendre-Gauss-Lobatto Pseudospectral collocation code developed at the Naval Postgraduate School, to solve the problem. Solutions obtained by this method are compared against a previous study. Key issues were checking the optimality of the solutions by way of the necessary conditions and the behavior of the solution to changes in the thruster size. The results confirmed Jensen's findings of propellant savings of one to five percent when compared against a middle altitude Forced Keplerian Trajectory (FKT). Larger savings are predicted if compared against a finite-burn Hohmann transfer with drag. The costates estimates compared favorably against necessary conditions of Pontryagin's Minimum Principle. Analysis of the switching function yielded periods of thrust-modulated arcs. The optimal thrust profile appears to be a thrust-modulated burn to raise the orbit followed by an orbital decay and a terminating thrust-modulated arc. For a sufficiently low thrust-control authority, the switching structure includes a maximum thrust arc. Indirect optimization techniques to confirm these findings were unsuccessful.</p>			
14. SUBJECT TERMS Orbital Mechanics, Optimization, Optimal Control Theory, Orbit Maintenance			15. NUMBER OF PAGES 93
			16. PRICE CODE
17. SECURITY CLASSIFI- CATION OF REPORT Unclassified	18. SECURITY CLASSIFI- CATION OF THIS PAGE Unclassified	19. SECURITY CLASSIFI- CATION OF ABSTRACT Unclassified	20. LIMITATION OF ABSTRACT UL

Approved for public release; distribution is unlimited

A NUMERICAL STUDY OF FUEL-OPTIMAL LOW-EARTH ORBIT MAINTENANCE

Lawrence E. Halbach
Major, United States Air Force
B.A.E.M., University of Minnesota, 1988

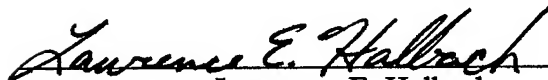
Submitted in partial fulfillment of the
requirements for the degree of

MASTER OF SCIENCE IN ASTRONAUTICAL ENGINEERING


from the

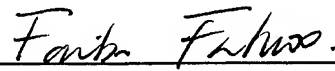
**NAVAL POSTGRADUATE SCHOOL
December 2000**

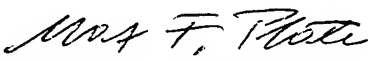
Author:


Lawrence E. Halbach

Approved by:


I. M. Ross, Thesis Advisor


Fariba Fahroo, Co-Advisor


Max F. Platz, Chairman
Department of Aeronautics and Astronautics

THIS PAGE INTENTIONALLY LEFT BLANK

ABSTRACT

This thesis studies the fuel optimal periodic reboost profile required to maintain a spacecraft experiencing drag in low-earth-orbit (LEO). Recent advances in computational optimal control theory are employed, along with a Legendre-Gauss-Lobatto Pseudospectral collocation code developed at the Naval Postgraduate School, to solve the problem. Solutions obtained by this method are compared against a previous study. Key issues were checking the optimality of the solutions by way of the necessary conditions and the behavior of the solution to changes in the thruster size. The results confirmed Jensen's findings of propellant savings of one to five percent when compared against a middle altitude Forced Keplerian Trajectory (FKT). Larger savings are predicted if compared against a finite-burn Hohmann transfer with drag. The costates estimates compared favorably against necessary conditions of Pontryagin's Minimum Principle. Analysis of the switching function yielded periods of thrust-modulated arcs. The optimal thrust profile appears to be a thrust-modulated burn to raise the orbit followed by an orbital decay and a terminating thrust-modulated arc. For a sufficiently low thrust-control authority, the switching structure includes a maximum thrust arc. Indirect optimization techniques to confirm these findings were unsuccessful.

THIS PAGE INTENTIONALLY LEFT BLANK

TABLE OF CONTENTS

I. INTRODUCTION.....	1
II. OPTIMIZATION THEORY AND PROBLEM FORMULATION.....	5
A. ORBITAL MAINTENANCE METHODS	5
B. OPTIMIZATION THEORY	8
C. PROBLEM FORMULATION.....	9
1. <i>Normalized Equations of Motion</i>	9
2. <i>Cost Function</i>	13
D. NUMERICAL DISCRETIZATION	14
III. LINEAR AND NONLINEAR ORBITAL EQUATIONS OF MOTION.....	17
A. LINEAR ORBITAL EQUATIONS - HILL'S EQUATIONS	17
1. <i>Hill's Equations of Motion</i>	17
2. <i>Normalization</i>	19
B. NONLINEAR ORBITAL EQUATIONS - BRYSON HO EXAMPLE	19
1. <i>Orbital Equations of Motion</i>	19
C. COMPARISON METHODOLOGIES	21
D. FIXED FINAL TIME - CONSTANT THRUST COMPARISONS	22
E. FREE FINAL TIME COMPARISONS	24
IV. DIRECT METHOD ANALYSIS	27
A. ANALYSIS METHODOLOGY	27
1. <i>Numerical Computation</i>	27
B. RESULTS.....	34
1. <i>Comparison to Jensen's Results</i>	34
2. <i>Effect of Final Time Constraint</i>	37
3. <i>Effect of Radius Constraint</i>	41
4. <i>Costates and Necessary Conditions</i>	43
C. NUMERICAL ANALYSIS ISSUES.....	57
1. <i>Effects of Problem Formulation</i>	57
2. <i>Stability of Solutions</i>	59
3. <i>Effect of Increasing the Number of LGL Points</i>	60
V. ANALYSIS BY AN INDIRECT METHOD.....	63
VI. ANALYSIS OF THE SWITCHING STRUCTURE.....	69
VII. CONCLUSIONS	75
LIST OF REFERENCES	77
INITIAL DISTRIBUTION LIST.....	79

THIS PAGE INTENTIONALLY LEFT BLANK

LIST OF FIGURES

Figure II-1 Hohmann Transfer	6
Figure II-2 Propellant Comparison from Jensen [Ref. 3]	7
Figure II-3 Geometry for Equations of Motion.....	10
Figure III-1 Geometry for Hill's Equations of Motion	18
Figure III-2 Geometry for Nonlinear Equations of Motion (from Bryson and Ho)	20
Figure III-3 States and Controls, $t_f=3.32$ (Bryson Ho Formulation)	23
Figure III-4 Hill's Equations States and Controls, $t_f=3.32$	24
Figure III-5 States and Controls, $R_f=1.525$, Free Final Time (Bryson Ho Formulation).....	26
Figure III-6 Hill's Equations States and Controls, $R_f=1.1$	26
Figure IV-1 <i>optmainfixed3.m</i> MATLAB script file	29
Figure IV-2 Nonlinear Constraints File, <i>optconfixed.m</i>	32
Figure IV-3 Cost Function File, <i>optobj.m</i>	33
Figure IV-4 Initial Guess Function, <i>optinitial.m</i>	34
Figure IV-5 States and Controls using NPSOL Solver ($t_f=112.6$, $n=30$).....	35
Figure IV-6 Periodic Reboost Cost Comparison	38
Figure IV-7 State and Control History, $t_f=80$	41
Figure IV-8 States and Controls for Altitude Limited Case ($t_f=700$, $n=50$)	42
Figure IV-9 Costates Generation Code	45
Figure IV-10 Plots of Costates ($n=30$, $t_f=112.6$).....	46
Figure IV-11 Filtered Costates for $n=30$	47
Figure IV-12 Switching Condition, S , and Thrust/1000.....	49
Figure IV-13 Switch and Thrust Using Filtered Costates.....	50
Figure IV-14 Optimality Condition, $\frac{\partial H}{\partial \varepsilon} = 0$	51
Figure IV-15 Plot of $\frac{\partial^2 H}{\partial \varepsilon^2}$	52
Figure IV-16 Plot of Hamiltonian.....	53
Figure IV-17 Costate Difference Plots, $\dot{\lambda}^T + \frac{\partial H}{\partial x} = 0$	55
Figure IV-18 Results from Modified Problem Formulation.....	58
Figure IV-19 Thrust Profile Comparison.....	58
Figure IV-20 Variations of $t_f=112.6$ Runs with Number of LGL Points	61
Figure IV-21 Variations of $t_f=80$ Runs with Number of LGL Points	61
Figure V-1 Thrust and Thrust Angle Equations.....	64
Figure V-2 Non-Convergent States and Controls, Convergent Measure = 0.0575	66
Figure V-3 Non-Convergent Costates, Convergent Measure = 0.0575	66
Figure V-4 Plot of Optimality Condition, $\frac{\partial H}{\partial \varepsilon}$	68
Figure V-5 Indirect Method Responses to Fixed Number of Iterations.....	68
Figure VI-1 Thrust Profiles for Increasing T_{\max} at final time of 700	70
Figure VI-2 Switching and Thrust for $T_{\max} = 5$ and $t_f = 700$	71

Figure VI-3 Switching and Thrust for $T_{\max} = 15$ and $t_f = 700$	71
Figure VI-4 Switching and Thrust for $T_{\max} = 50$ and $t_f = 700$	72
Figure VI-5 Switching and Thrust for $T_{\max} = 100$ and $t_f = 700$	73

LIST OF TABLES

Table II-1 Generic Spacecraft Characteristics from Jensen [Ref. 3].....	13
Table II-2. Ballistic Coefficients from Jensen [Ref. 3].....	13
Table III-1 Fixed Final Time Comparison from NPSOL.....	22
Table III-2 Free Final Time Comparison	25
Table IV-1 Mid-FKT Cost Analysis	40

THIS PAGE INTENTIONALLY LEFT BLANK

I. INTRODUCTION

Orbiting spacecraft experience a number of orbit perturbations, which usually require thruster firings to correct. These thruster firings use propellant, which is a non-replaceable resource in the spacecraft and often limits the mission duration. This thesis presents a numerical study of an optimal periodic thrusting method for low earth orbits for which drag is the primary orbital perturbation.

Conventional thinking holds that the Hohmann transfer is the minimum energy transfer method, and hence, optimal. While this may be true for exoatmospheric orbits and ideal thrusters in which the impulse is applied instantaneously, it is not necessarily true for spacecraft in low earth orbit (LEO) with finite-burn thrusters. In fact, Ross and Alfrend have shown that there exists an orbit transfer method that is more efficient than a Hohmann transfer [Ref. 1]. Ross [Ref. 2] also showed that optimal endoatmospheric maneuvers generally contain "singular thrust arcs". To quantitatively determine the optimal orbital maintenance maneuver, Jensen [Ref. 3] numerically investigated the problem based on algorithms developed by Fahroo and Ross [Ref. 4]. Part of this thesis is a follow-on to that analysis and seeks to confirm those findings using different numerical tools developed at the Naval Postgraduate School (NPS).

An optimal orbital control methodology has potential to save thousands of dollars in launch costs and/or increase mission durations. This is particularly important considering the large number of spacecraft and constellations of spacecraft planned for low earth orbit. The propellant savings may be used directly to reduce spacecraft launch

mass at a savings of approximately \$10,000 per kilogram [Ref. 3], or, the same amount of propellant may be launched, but the mission duration extended. Either of these are significant enough benefits to pursue this investigation.

The optimal control analysis starts with the equations of motion and a cost function. The equations of motion describe the physical system. The cost function describes the amount of propellant consumed. The objective is to minimize the cost function consistent with the physical limitations of the system.

Chapter II of this thesis contains a description of key concepts and methodologies along with the problem formulation for the optimal control problem. It first describes two different orbit transfer methods that are used for comparison to the optimal control method derived later. Optimal control theory is described along with a spectral collocation method used to discretize the problem for numerical analysis. Finally, the specific problem to be solved is formulated.

Chapter III contains analysis performed on the use of linear versus non-linear equations in formulating orbital problems. This chapter studies and compares the use of Hill's linear equations of relative motion and the more typical nonlinear equations of motion. [Ref. 5] A well-known problem from Bryson and Ho is solved to confirm the solutions for the nonlinear equations. [Ref. 6] The linear equations are investigated to see if they provide a suitable replacement for the nonlinear equations. If so, this may benefit the numerical analysis by simplifying the equations of motion and possibly reducing computational time.

Chapter IV contains results from analysis using the direct method of optimization. The numerical analysis methodology is described along with the resulting optimal states, costates, and costs. The resultant states and controls are then compared against the necessary conditions described in Chapter II. Issues encountered during the numerical analysis conclude this chapter.

Chapter V discusses the attempted implementation of an indirect method of optimization. A converged solutions was not obtained, so the "best" answer obtained is discussed along with the numerical analysis issues encountered.

Chapter VI briefly looks at the thrust profiles. Some profiles encountered in this analysis were bang-bang while others followed singular arcs. This chapter relates those results to the switching function, which is obtained from the optimality conditions described in Chapter II.

The thesis ends with a summary of major findings and conclusions.

THIS PAGE INTENTIONALLY LEFT BLANK

II. OPTIMIZATION THEORY AND PROBLEM FORMULATION

A. ORBITAL MAINTENANCE METHODS

Spacecraft orbits are perturbed by a number of forces and the magnitude of these perturbations depend upon the specific orbit and spacecraft. This study looks at the impact of drag on low earth orbiting spacecraft and coplanar orbital transfer methods to counter the orbit decay caused by drag.

Three different orbital maintenance methods are described here. These include the Hohmann Transfer, the forced Keplerian trajectory (FKT), and the periodic reboost. The Hohmann transfer boosts a spacecraft from one circular orbit to a different circular orbit using two boosts or thrustings. The FKT applies enough thrust to counter the drag so that thrust equals drag continuously. The periodic reboost does multiple burns to maintain boundary conditions and the number of burns are determined by a switching function. Both the Hohmann and periodic reboost method rely on boosting to a higher altitude and slowly decaying back to the original altitude at which time the maneuvers are repeated.

The Hohmann transfer has long been considered the minimum energy or most efficient transfer method [Ref. 5]. It transfers a spacecraft between two orbits by using two tangential thrusts as shown in Figure II-1. The first burn, Δv_a , places the spacecraft into an elliptical orbit and the second burn, Δv_b , circularizes the orbit at the final altitude.

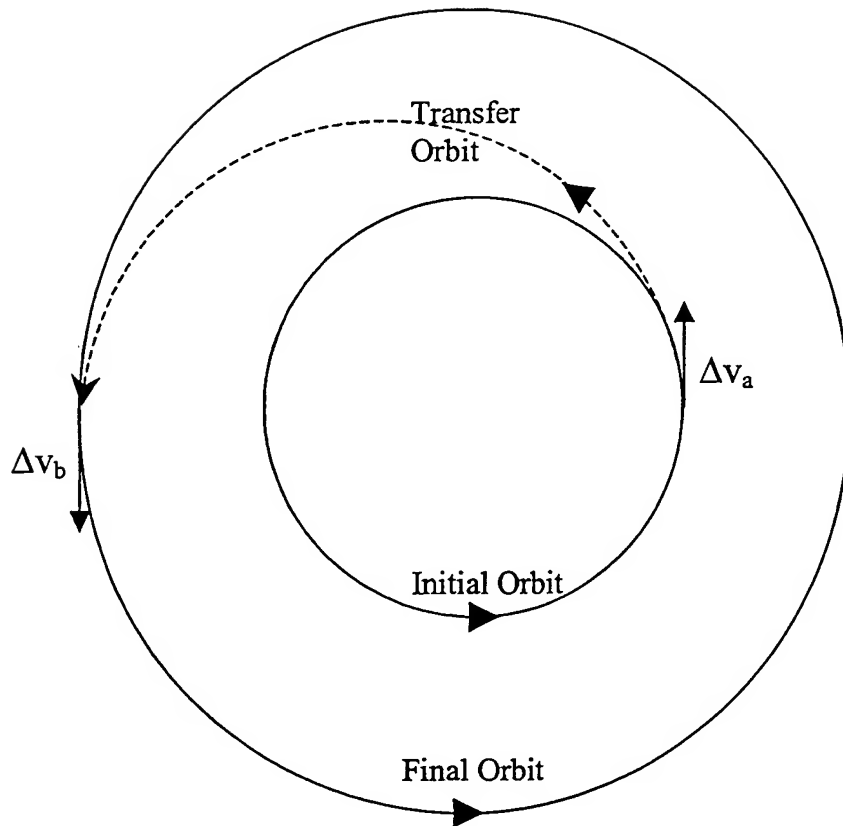


Figure II-1 Hohmann Transfer

The FKT uses a drag cancellation process in which the thrust is continuously throttled to counter the force of drag. This requires the thruster to operate continuously at different thrust levels. Drag is a function of the local density (ρ), the orbital velocity (v), the area of the spacecraft in the direction of motion (A), and the coefficient of drag (C_D) ($\text{Drag} = C_D A \rho v^2 / 2$). Since density varies during an orbit, the thrust level must be variable to exactly counter the varying drag force.

The FKT varies with altitude and will be called either a low, mid, or high FKT. A low-FKT is an FKT performed at the initial altitude from which the Hohmann and periodic reboost transfers begin. The mid-FKT occurs at the altitude midway between the

initial and the highest orbit obtained by the Hohmann or periodic reboost. The high-FKT occurs at the highest altitude obtained by a comparable Hohmann or periodic reboost.

The ideal Hohmann is closely approximated by the mid-FKT [Ref 1,3]. The low-FKT uses more fuel than the Hohmann while the high-FKT uses less fuel. Figure II-2 is from Jensen and gives a comparison of the propellant usage by each type [Ref. 3].

If there are no state constraints, it has been shown that the FKT is not the fuel optimal solution [Ref. 1]. Since the Hohmann transfer does not do better than the mid-FKT, the Hohmann reboost cannot be the fuel optimal solution either. This thesis attempts to identify an optimal periodic transfer that is more efficient.

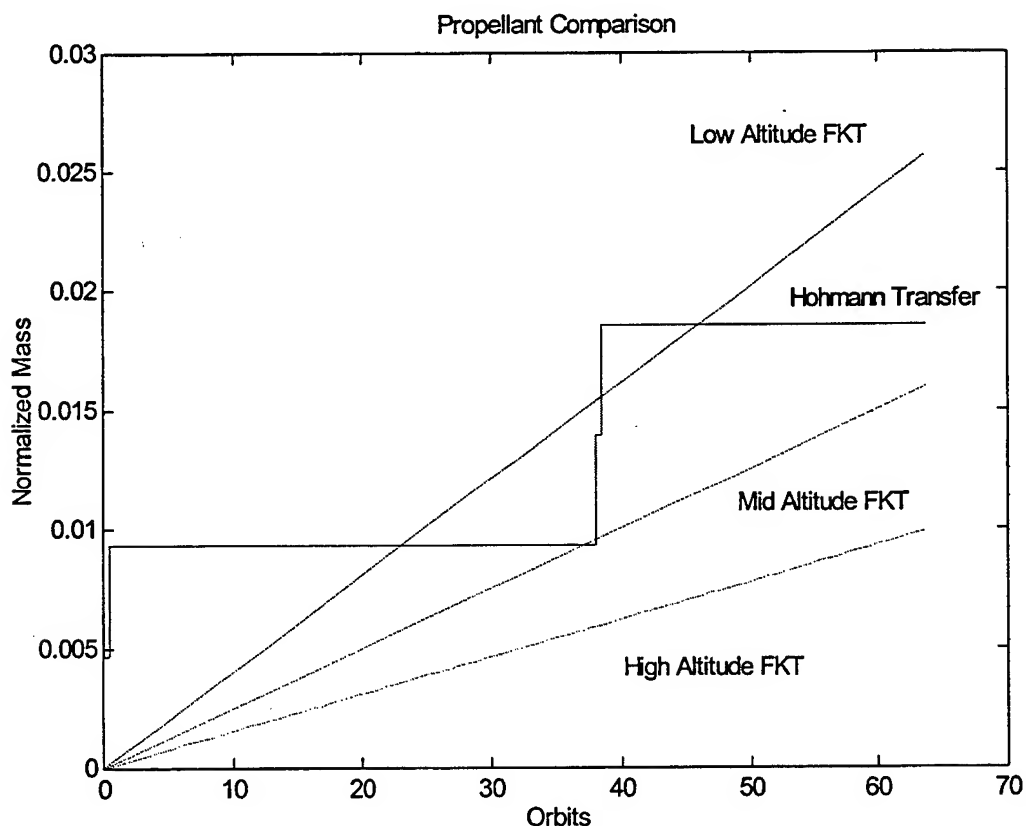


Figure II-2 Propellant Comparison from Jensen [from Ref. 3]

B. OPTIMIZATION THEORY

The optimization problem is generally formulated by a system of state equations and a cost function. These equations are functions of the states (\mathbf{x}), controls (\mathbf{u}), and time (t). The problem is usually stated in the following manner. [Ref. 7] Given a dynamical system given by

$$\dot{\mathbf{x}} = \mathbf{f}(\mathbf{x}, \mathbf{u}, t)$$

where **boldface** indicates vectors, determine the optimal control history, \mathbf{u}^* , which transfers the state of the system from its initial conditions to a final target, $\psi(\mathbf{x}_f, t_f)$ while minimizing the performance index (or cost), J , given by:

$$J[\mathbf{u}] = M(\mathbf{x}_f, t_f) + \int_{t_0}^{t_f} L(\mathbf{x}, \mathbf{u}, t) dt \quad [\text{Ref. 8}]$$

Pontryagin's Minimum Principle provides the necessary conditions for optimality [Ref. 8]. The Hamiltonian, is constructed from the cost function (L) with the introduction of costates (λ) given by:

$$H = L(\mathbf{x}, \mathbf{u}, t) + \lambda^T \mathbf{f}(\mathbf{x}, \mathbf{u}, t)$$

The costates satisfy the following differential equation:

$$\dot{\lambda} = -\frac{\partial H}{\partial \mathbf{x}} \quad (\text{II-1})$$

The Minimum Principle states that the optimal control, \mathbf{u}^* , minimizes H at every point on the trajectory. For example, if there are no constraints on the controller then we must have

$$\frac{\partial H}{\partial \mathbf{u}} = 0 \quad (\text{II-2})$$

and

$$\frac{\partial^2 H}{\partial \mathbf{u}^2} \geq 0 \quad (\text{II-3})$$

The final conditions on the costates are obtained from the transversality equations [Ref. 8]

$$\lambda(t_f) = \frac{\partial M}{\partial \mathbf{x}_f} + \left(\frac{\partial \psi}{\partial \mathbf{x}_f} \right)^T \mathbf{v}_f \quad (\text{II-4})$$

$$H(t_f) + \frac{\partial M(t_f)}{\partial t_f} + \mathbf{v}_f^T \frac{\partial \psi(t_f)}{\partial t_f} = 0 \quad (\text{II-5})$$

where $\psi(\mathbf{x}(t_f), t_f) = \mathbf{0}$ defines the target states.

C. PROBLEM FORMULATION

The basic problem studied in Chapters IV through VI is a constrained optimization problem with both equality and inequality constraints. The cost function is of the Lagrangian form in which the cost is an integral in time. The five equations of motion detailed below in section 1 are the state equations of the form $\dot{\mathbf{x}} = \mathbf{f}$ where $\dot{\mathbf{x}}$ is a vector containing the first order state equations. State constraints $\mathbf{h}(\mathbf{x})$ and control constraints $\mathbf{g}(\mathbf{u})$ also exist and may be equality ($= 0$) or inequality constraints (≤ 0).

1. Normalized Equations of Motion

The orbital equations of motion are first order ordinary differential equations. The equations are written for a coplanar low earth orbit in which drag (D) has a significant

effect on the orbit. A summary of the normalization process performed in Reference 3 is provided here.

The first order equations of motion are based on the geometry in Figure II-3.

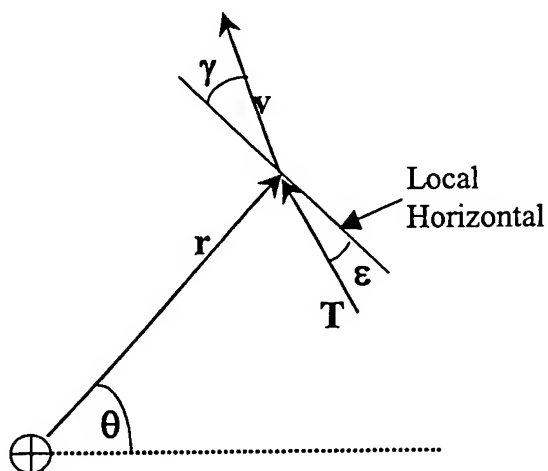


Figure II-3 Geometry for Equations of Motion

The five equations of motion contain five states; radius (r), velocity (v), flight path angle (γ), mass (m), and a reference angle (θ), and two controls; thrust (T) and thrust angle (ϵ) and are given by

$$\dot{r} = v \sin(\gamma) \quad (\text{II-6})$$

$$\dot{v} = \frac{T \cos(\epsilon) - D}{m} - g \sin(\gamma) \quad (\text{II-7})$$

$$\dot{\gamma} = \left(\frac{v^2}{r} - g \right) \frac{\cos(\gamma)}{v} + \frac{T \sin(\epsilon)}{mv} \quad (\text{II-8})$$

$$\dot{m} = \frac{-T}{v_e} \quad (\text{II-9})$$

$$\dot{\theta} = \frac{v \cos(\gamma)}{r} \quad (\text{II-10})$$

When thrust (T) is normalized to a reference drag force, it allows a more intuitive interpretation of the results. A normalized thrust of one means the thrust equals the reference drag. A normalized thrust of 5 means the thrust is 5 times the force of the reference drag.

The reference drag force is defined by the basic aerodynamic equation of drag given by

$$D_{\text{ref}} = \frac{1}{2} \rho_{\text{ref}} C_D A v^2 \quad (\text{II-11})$$

In this equation, the density ρ_{ref} and the orbital velocity, v , are both at the reference altitude. The coefficient of drag, C_D , and area, A , are both physical characteristics of the spacecraft.

The ballistic coefficient, B , of the spacecraft is also used to simplify the normalized equations. The ballistic coefficient is a function of the spacecraft's mass, coefficient of drag, and area (in the direction of velocity) and is given by

$$B = \frac{m}{C_D A} \quad (\text{II-12})$$

If the ballistic coefficient is nondimensionalized by

$$\bar{B} = \frac{B}{\left(\frac{r_{\text{ref}} \rho_{\text{ref}}}{2} \right)} \quad (\text{II-13})$$

then the equations of motion normalize to

$$\dot{\bar{r}} = \bar{v} \cdot \sin(\gamma) \quad (\text{II-14})$$

$$\dot{\bar{v}} = -\bar{g} \cdot \sin(\gamma) + \frac{\bar{T} \cdot \cos(\epsilon) - \bar{D}}{\bar{m} \bar{B}} \quad (\text{II-15})$$

$$\dot{\gamma} = \left(\frac{\bar{v}^2}{\bar{r}} - \bar{g} \right) \cdot \frac{\cos(\gamma)}{\bar{v}} + \frac{\bar{T} \cdot \sin(\varepsilon)}{\bar{m} \cdot \bar{v} \cdot \bar{B}} \quad (\text{II-16})$$

$$\dot{\bar{m}} = \frac{-\bar{T}}{v_e \bar{B}} \quad (\text{II-17})$$

$$\dot{\theta} = \frac{\bar{v}}{\bar{r}} \cdot \cos(\gamma) \quad (\text{II-18})$$

The state constraints for $(r, v, \gamma, m, \theta)$ are

$$r(0) - r(t_f) = 0 \quad v(0) - v(t_f) = 0 \quad \gamma(0) - \gamma(t_f) = 0$$

$$\frac{-\pi}{2} \leq \gamma \leq \frac{\pi}{2}$$

$$0 \leq \bar{m} \leq 1 \quad (\text{normalized mass})$$

$$0 \leq \theta$$

The control constraints for (T, ε) are

$$0 \leq \bar{T} \leq 5 \quad (\text{normalized thrust})$$

$$-\pi \leq \varepsilon \leq \pi$$

A generic spacecraft that experiences major disturbances due to drag is used in this study and is the same one used by Jensen [Ref. 3]. The specifications of this spacecraft, along with the normalized value where appropriate, are given in Table II-1. As a comparison, the normalized ballistic coefficients for some real spacecraft are included in Table II-2.

Table II-1 Generic Spacecraft Characteristics from Jensen [from Ref. 3]

	Physical Units	Normalized Units
Area	500 m ²	
Initial Mass	3000 kg	1
Maximum Thrust	3.5 N	5.0
Initial Radius	6678.15 km	1
Coefficient of Drag	2.35	
Ballistic Coefficient	2.55 kg/m ²	40890
Initial Orbit Radius	6678.15 km	1

Table II-2. Ballistic Coefficients from Jensen [from Ref. 3]

Generic Spacecraft	4.089*10 ⁴
ISS-DACT 6	1.26*10 ⁶
Space Telescope	4.72*10 ⁵
Landsat-1	4.04*10 ⁵
Echo-1	8.24*10 ²

2. Cost Function

The objective is to minimize the amount of propellant required over a given period to maintain the orbit at or above the desired orbit radius. Therefore the cost is related to the change in mass divided by the change in time. The periodic cost function, J_p , is given by

$$J_p = \frac{m(0) - m(t_f)}{t_f} \quad (\text{II-19})$$

where t_f is the final time of the control period. Since thrust can be written as:

$$T = -\dot{m}v_e \quad (\text{II-20})$$

The cost function is rewritten as

$$J_p = \frac{1}{t_f} \int_0^{t_f} \frac{T}{v_e} dt \quad (\text{II-21})$$

In terms of the non-dimensional (or normalized) variables, the periodic cost function becomes:

$$J_p = \frac{1}{t_f} \int_0^{t_f} \frac{\bar{T}}{v_e B} dt \quad (\text{II-22})$$

As discussed earlier in this thesis, the Hohmann and FKT orbit maintenance methods are not the most fuel efficient maneuvers. The cost function for an FKT trajectory is similar to the periodic cost function but with the additional refinement that the thrust equals the drag. So, the normalized thrust (normalized to drag) is equal to one. The FKT cost function then becomes:

$$J_{\text{FKT}} = \frac{1}{t_f} \int_0^{t_f} \frac{1}{v_e B} dt \quad (\text{II-23})$$

A ratio of these two cost functions provides an immediate indication of the performance of the periodic optimal control problem. If the ratio of the periodic cost to the FKT cost is less than one, then the periodic cost is more efficient than a low-FKT. The cost function then becomes.

$$J = \frac{1}{t_f} \int_0^{t_f} \bar{T} dt \quad (\text{II-24})$$

D. NUMERICAL DISCRETIZATION

A Legendre Pseudospectral method [Ref. 4] is used to formulate the periodic reboost problem for numerical analysis. This method uses polynomial approximations for the state and control functions and evaluates them at the Legendre-Gauss-Lobatto (LGL)

points. Discretizing the continuous problem into a finite dimensional nonlinear programming (NLP) formulation is necessary for numerical analysis.

The LGL points lie within the interval $[-1,1]$. A transformation [Ref. 4] is used to change the cost, state, and final conditions from the interval $[0, t_f]$ to the interval $[-1,1]$ resulting in the following cost and state equations

$$J = \frac{1}{2} \int_{-1}^1 \bar{T} dt \quad (\text{II-25})$$

$$\dot{\mathbf{x}}(t) = \left(\frac{t_f}{2} \right) \mathbf{f}(\mathbf{x}(t), \mathbf{u}(t)) \quad (\text{II-26})$$

or

$$\left(\frac{2}{t_f} \right) \dot{\mathbf{x}}(t) = \mathbf{f}(\mathbf{x}(t), \mathbf{u}(t)) \quad (\text{II-27})$$

This thesis addresses a periodic problem with periodic boundary conditions $\mathbf{x}(0)=\mathbf{x}(t_f)$. These boundary conditions become:

$$\mathbf{x}(-1) = \mathbf{x}(1) \quad (\text{II-28})$$

The state and control variables are approximated by N^{th} order Lagrange interpolating polynomials on the interval $[-1,1]$. It can be shown [Ref. 4] that the cost function in Equation II-25 can be rewritten in the following form.

$$J = \frac{1}{2} \sum_{k=0}^N w_k \cdot T_k \quad (\text{II-29})$$

where w_k are the LGL weights and T_k are the values of thrust at each LGL point for $k=0,\dots,N$.

The cost is now a discretized form of the integral in Equation II-25. The state dynamics may be discretized as

$$A_k = \frac{\tau}{2} f(a_k, b_k) - c_k = 0$$

where $c_k = \sum_{j=0}^N D_{kj} a_j$ for $k=0,\dots,N$, D_{kj} are the elements of the differentiation matrix, w_k are the LGL weights, and a_k and b_k are the values of the states and controls at t_k , respectively.

Similarly the system constraints can be approximated in the same manner.

$$B_k = g(a_k, b_k) \leq 0 \quad (\text{II-30})$$

As can be seen from the above equation, this method of discretization retains much of the structure of the continuous problem and allows for easy numerical analysis. The code that implements this method is known as DIDO and was developed by Professors Fahroo and Ross at the Naval Postgraduate School (NPS). A front-end graphical user interface (GUI) was developed by Hall [Ref. 9] as part of his M.S. Thesis. In this thesis, both the GUI and non-GUI versions of DIDO were employed to simulate all the direct solutions.

III. LINEAR AND NONLINEAR ORBITAL EQUATIONS OF MOTION

A. LINEAR ORBITAL EQUATIONS - HILL'S EQUATIONS

1. Hill's Equations of Motion

Hill's equations [Ref. 5] are useful in describing the relative motion between two close-orbiting satellites. The geometry is provided in Figure III-1. The satellite's position is measured in terms of its original location, which is moving in the initial circular orbit. The coordinates (x,y) are always referenced to this initial, though moving, point. The x coordinate is collinear with the position vector of the initial point. The y coordinate is in the direction of motion of the initial point and aligned with the local horizontal.

Figure III-1 shows the changing geometry of the scenario. Point 1 is the position in the initial orbit at which the maneuver begins and has unit direction vectors x_1 and y_1 . At some later time, the origin has moved to point 2 and the spacecraft position is measured in terms of x_2 and y_2 . The spacecraft has moved from the initial circular orbit to the final circular orbit. The angle ϕ is the angle between the vector to the spacecraft position and the vector to the current position of the x,y origin.

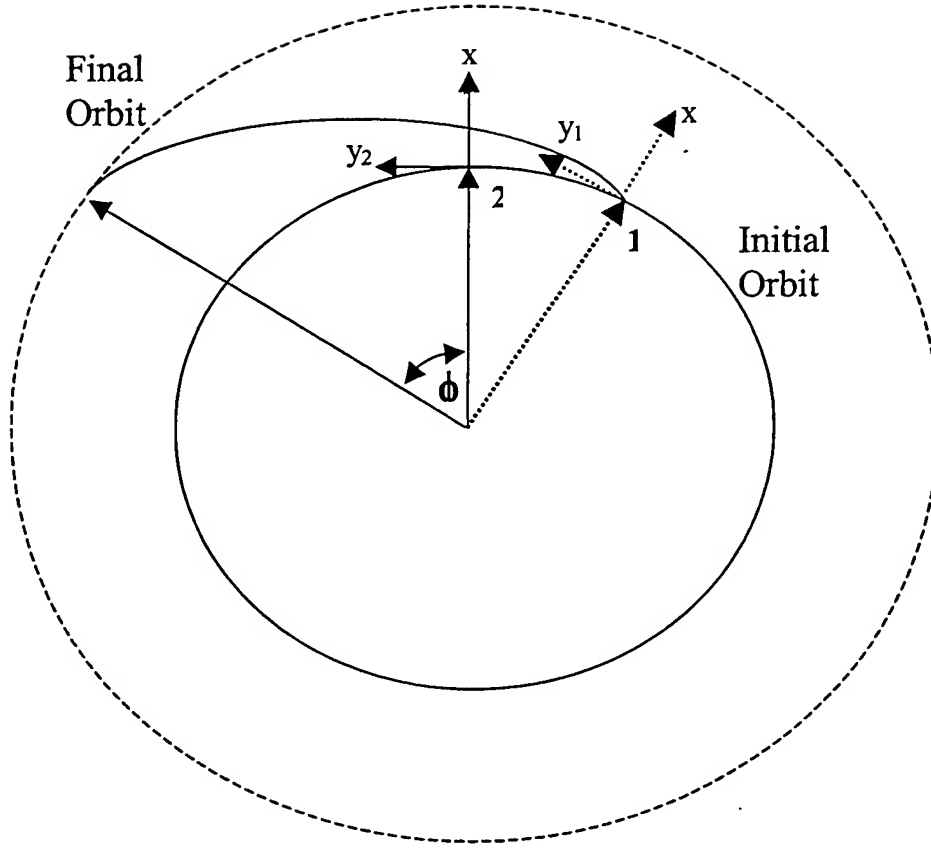


Figure III-1 Geometry for Hill's Equations of Motion

The equations of motion are developed by analysis of relative positions and velocities as described by Vallado. [Ref. 5] After reducing to first order differential equations, the two dimensional equations are given by

$$\dot{x} = V_x \quad (\text{III-1})$$

$$\dot{V}_x = 2\omega V_y + 3\omega^2 x + f_x = 2\omega V_y + 3\omega^2 x + \frac{T}{m} \sin(\varepsilon) \quad (\text{III-2})$$

$$\dot{y} = V_y \quad (\text{III-3})$$

$$\dot{V}_y = -2\omega V_x + f_y = -2\omega V_x + \frac{T}{m} \cos(\varepsilon) \quad (\text{III-4})$$

$$\dot{m} = \frac{-T}{v_e} \quad (\text{III-5})$$

2. Normalization

A normalization was performed using the initial orbit radius and velocity as references. A reference radius, r_{ref} , was defined as the initial orbit radius. A reference time, t_{ref} , and a reference velocity, v_{ref} , defined by

$$t_{\text{ref}} = \sqrt{\frac{r_{\text{ref}}^3}{\mu}} \quad (\text{III-6})$$

$$v_{\text{ref}} = \sqrt{\frac{\mu}{r_{\text{ref}}}} \quad (\text{III-7})$$

permit the equations to be normalized as

$$\dot{\bar{x}} = \bar{V}_x \quad (\text{III-8})$$

$$\dot{\bar{V}}_x = 2\bar{\omega}\bar{V}_y + 3\bar{\omega}^2\bar{x} + \frac{\bar{T}}{\bar{m}}\sin(\varepsilon) \quad (\text{III-9})$$

$$\dot{\bar{y}} = \bar{V}_y \quad (\text{III-10})$$

$$\dot{\bar{V}}_y = -2\bar{\omega}\bar{V}_x + \frac{\bar{T}}{\bar{m}}\cos(\varepsilon) \quad (\text{III-11})$$

$$\dot{\bar{m}} = -\left(\frac{\bar{T}}{\bar{v}_e}\right) \quad (\text{III-12})$$

B. NONLINEAR ORBITAL EQUATIONS - BRYSON HO EXAMPLE

1. Orbital Equations of Motion

Bryson and Ho [Ref. 6] present a nonlinear orbit transfer formulation using constant thrust for a fixed time. This problem has been solved and a "known" answer is used as a baseline for comparison. The orbit geometry is presented in Figure III-2. The

thrust angle, ϕ , has been replaced with ε to correlate with Hill's equations previously developed.

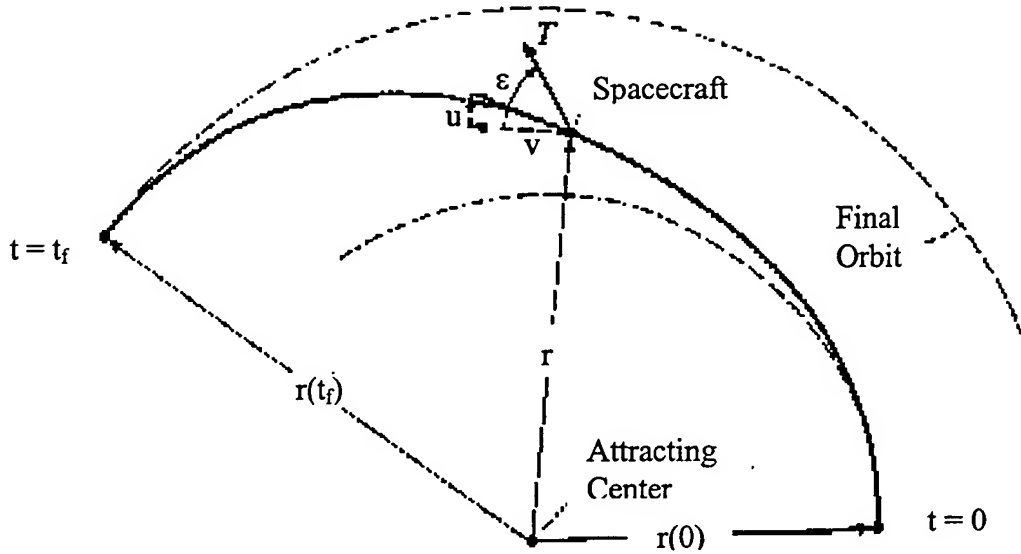


Figure III-2 Geometry for Nonlinear Equations of Motion (from Bryson and Ho)

A modified formulation allowing for variable thrust results in the following normalized equations of motion

$$\dot{r} = u \quad (\text{III-13})$$

$$\dot{u} = \frac{v^2}{r} - \frac{\mu}{r^2} + \frac{T \sin(\varepsilon)}{m} \quad (\text{III-14})$$

$$\dot{v} = -\frac{uv}{r} + \frac{T \cos(\varepsilon)}{m} \quad (\text{III-15})$$

$$\dot{m} = \frac{-T}{v_e} \quad (\text{III-16})$$

where $0 \leq T \leq 0.1405$ (variable thrust formulation)

Note that in Bryson and Ho, the thrust is constant at $T = 0.1405$

C. COMPARISON METHODOLOGIES

The linear and nonlinear formulations discussed above were compared for two different problem formulations; free final time and fixed final time. In the free final time formulation, the objective is to minimize the transfer time from one circular orbit to another circular orbit using thrust and thrust angle as controls. In the fixed final time formulation, the objective is to maximize the orbit radius using constant maximum thrust and only the thrust angle as a control.

The case to be studied consists of an orbit transfer from one circular orbit to another. The nondimensional orbit has an initial orbit radius of one ($r=1$) and an initial transverse velocity of one ($v=1$) in non-dimensional units. The thrust is modeled as a nondimensional quantity equal to 0.1405 for the constant thrust scenario. In the cases where thrust is a control variable, it is limited between zero and 0.1405.

The final time conditions ensure that the final velocities $V_x(t_f)$ and $V_y(t_f)$ correspond to a circular orbit and must be written in terms of the velocity with respect to the central body, such as the earth. These final time conditions are

$$V_x(t_f) = -\sqrt{\frac{1}{r}} \cdot \sin(\varepsilon) + \omega_0 y(t_f) \quad (\text{III-17})$$

$$V_y(t_f) = \sqrt{\frac{1}{r}} \cdot \cos(\varepsilon) - \sqrt{\frac{1}{R}} - \omega_0 x(t_f) \quad (\text{III-18})$$

The cost function (costfn) is the final radius. Maximizing the final radius is the same as minimizing the negative final radius.

D. FIXED FINAL TIME - CONSTANT THRUST COMPARISONS

The fixed final time comparisons are based upon the final radius obtained using Hill's equations and the Bryson and Ho problem. The analysis began by running the same problem as Bryson and Ho, that is, continuous thrust with final time (t_f) equal to 3.32 to see if the same results were obtained. The standard answer given by Bryson and Ho is a final radius of 1.525. By comparison, DIDO generated a final radius of 1.52 for the Bryson Ho formulation and 1.4964 for Hill's formulation. This validated the Bryson Ho program files.

Further solutions were obtained for times less than the original final time of 3.32. The results are provided below. The percent difference is the amount by which the Hill's solution differed from the Bryson Ho formulation. These answers are for $n=60$ LGL points.

Table III-1 Fixed Final Time Comparison from NPSOL

Final Time	Final Radius		Percent Difference
	Bryson Ho	Hill	
3.32	1.52	1.4964	1.55 %
2.5	1.2772	1.3169	3.11 %
2	1.1568	1.1755	1.62 %

The results are very good. It appears the linear equations provide answers that closely approximate the nonlinear equations. Typically, linear equations are simpler and faster to solve. The use of Hill's linear equations may provide a suitable substitute for the

nonlinear equations to obtain quick approximations for the Bryson and Ho formulation.

Similar performance against other problem formulations is not assumed.

Figure III-3 contains the results of the Bryson Ho formulation for $t_f=3.32$ and Figure III-4 contains the results of the Hill's formulation for the same final time, $t_f=3.32$.

The radius and thrust angle curves are similar. The Bryson Ho formulation provides the radial and transverse velocity states. The Hill formulation provides the x and y states which are plotted together. The angle ϕ is derived from the x and y states. The radius plot in Figure III-4 is derived from

$$r = \sqrt{(1+x)^2 + y^2} \quad (\text{III-19})$$

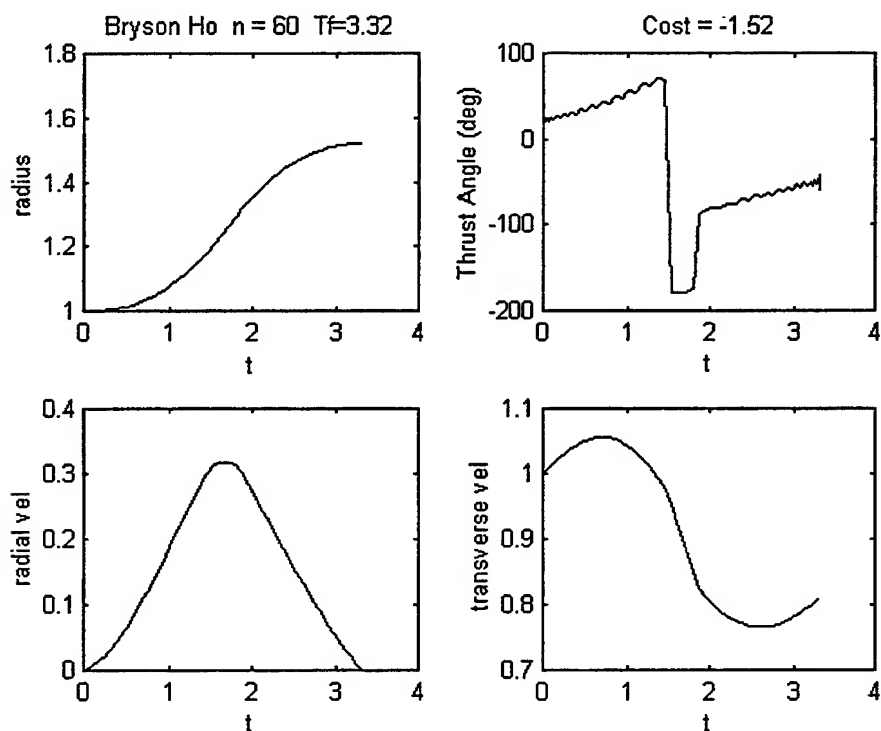


Figure III-3 States and Controls, $t_f=3.32$ (Bryson Ho Formulation)

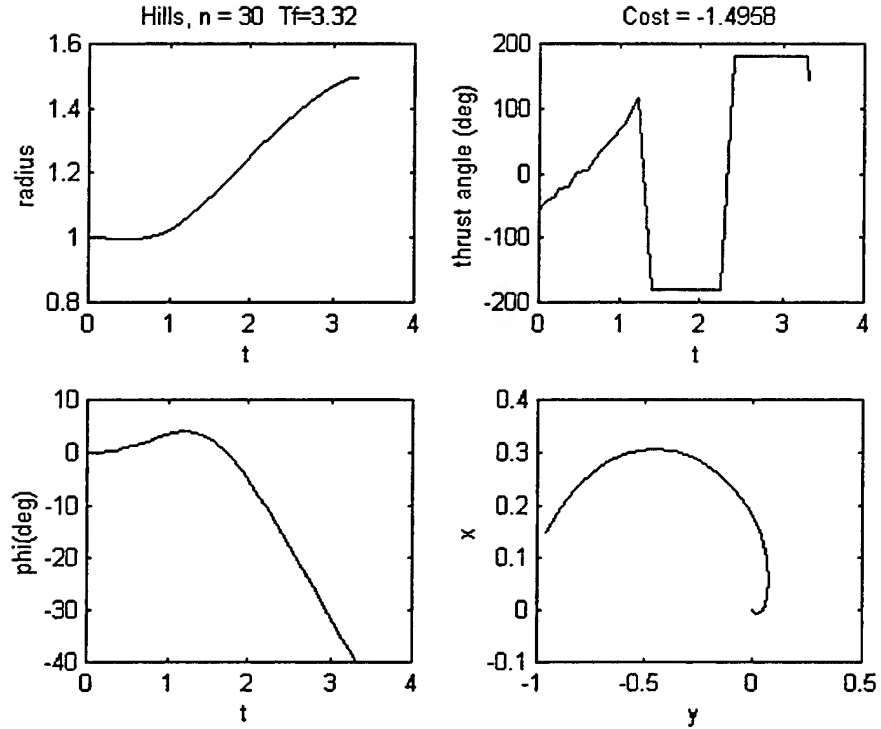


Figure III-4 Hill's Equations States and Controls, $t_f=3.32$

E. FREE FINAL TIME COMPARISONS

In the free final time analysis, the final radius is fixed and the program optimizes (minimizes) the amount of time to reach that orbit. Both thrust and thrust angle are control variables. Unlike the constant thrust used in the fixed time analysis, the thrust may vary within the constraints described by

$$0 \leq T \leq 0.1405$$

The results of several runs at different final radii are given in Table III-2.

Table III-2 Free Final Time Comparison

Final Radius	Final Time		Percent Difference
	Bryson Ho	Hill	
1.05	1.1455	1.1922	4.08%
1.1	1.6182	1.5807	2.32%
1.3	2.5917	2.3829	8.06%
1.525	3.3194	3.4944	5.28%
2	4.6504		
2.5	5.8054		
3	7.8518		
3.5	7.5065		

A solution to the Hill's equations for final radius larger than 1.5 could not be obtained. The difference between the Bryson Ho solutions and the Hill's solutions increased slightly as the final radius increased. This indicates that the linear Hill's equations appear to have a limitation beyond which they are not a reliable replacement for the more robust nonlinear equations. A larger problem was the inability to obtain a solution using the Hill formulation for radii larger than 1.5.

Examples of the states and controls for both formulation types are shown in Figures III-5 and III-6. The free final time results using the Bryson Ho formulation in Figure III-5 compare very well against the fixed final time results given in Figure III-3. The radius, thrust, thrust angle, and mass profiles are nearly identical. The results from the Hill formulation shown in Figure III-6 show trajectories with the same general shape as the Bryson Ho formulation. From this analysis, it appears that Hill's linear equations provide reasonable approximations to the Bryson Ho formulation for radii less than 1.5.

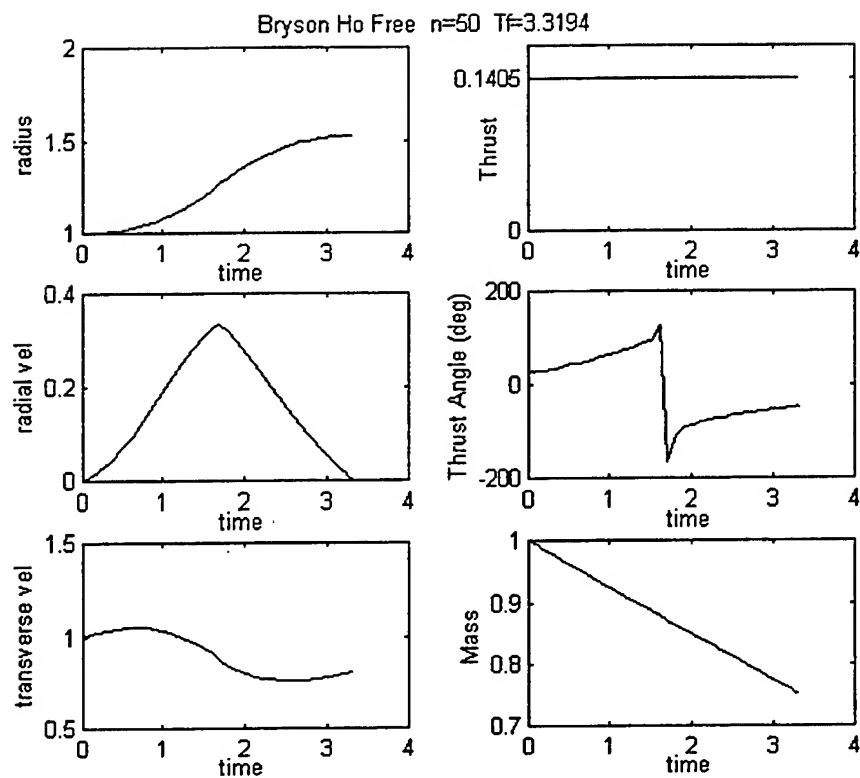


Figure III-5 States and Controls, $R_f=1.525$, Free Final Time (Bryson Ho Formulation)

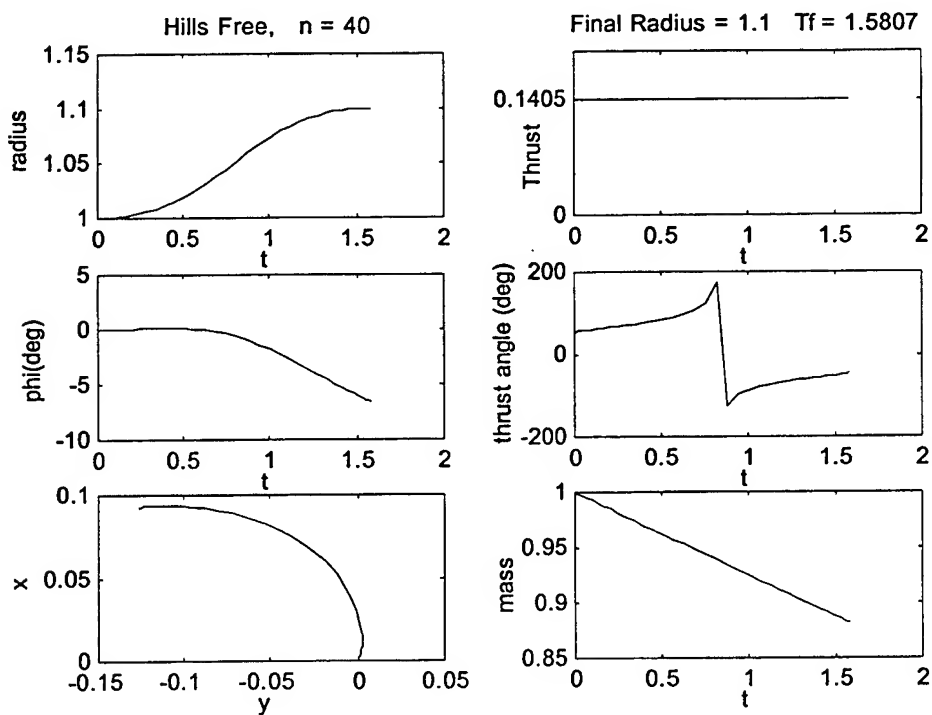


Figure III-6 Hill's Equations States and Controls, $R_f=1.1$

IV. DIRECT METHOD ANALYSIS

A. ANALYSIS METHODOLOGY

The problem formulated in Chapter II was solved numerically and then checked against Pontryagin's Minimum Principle (PMP). The numerical solution was obtained using MATLAB and NPSOL in the MATLAB environment. [Ref 11] The outputs of this solution are then used to determine if the optimal control solution, u^* , satisfies the PMP.

1. Numerical Computation

The NLP resulting from the LGL pseudospectral discretization was solved using the NPSOL software. The NLP problem must be stated in the form: minimize $f(x)$ subject to the constraints $l \leq k(x) \leq u$ where

$$k(x) = \begin{pmatrix} x \\ Ax \\ c(x) \end{pmatrix}$$

The vector x is a set of states and controls (called x_{opt} in this analysis), $f(x)$ is a nonlinear function, A is a matrix that accounts for linear constraints, and $c(x)$ is a vector of nonlinear functions/constraints. The functions $f(x)$ and $c(x)$ are assumed to be smooth, i.e., at least twice-continuously differentiable.

The problem, as defined above, was input into four different MATLAB script files: *optmainfixed3.m*, *optconfixed.m*, *optobj.m*, and *optinitialfixed.m*. The file *optmainfixed3.m* is run from the MATLAB command line and calls the others, along with the NPSOL software, when needed.

The *optmainfixed3.m* file is formatted as specified in the NPSOL user's manual. The entire file is given in Figure IV-1. The key parts are marked with large bold Roman numerals. Part I defines the A matrix. This matrix accounts for the linear constraints and is generally of the form $A * x_{opt} \leq b$, but for this problem it is $A * x_{opt} = 0$. The matrix A is an $(m \times k * n)$ dimensional matrix where m is the number of linear constraint equations, n is the number of LGL points, and k is the total number of states plus controls (7 in this problem). For this problem, the A matrix is used for the linear periodic constraints: $r(0)-r(t_f)=0$, $v(0)-v(t_f)=0$, and $\gamma(0) - \gamma(t_f) = 0$.

The x_{opt} vector contains the values of each state and control at each LGL point. This vector will eventually contain the optimized state and control histories at the n LGL points (see below).

$$\overline{x_{opt}} = \left\{ \begin{array}{c} r(1) \\ \cdot \\ r(n) \\ v(1) \\ \cdot \\ v(n) \\ \gamma(1) \\ \cdot \\ \gamma(n) \\ m(1) \\ \cdot \\ m(n) \\ T(1) \\ \cdot \\ T(n) \\ \epsilon(1) \\ \cdot \\ \epsilon(n) \\ \theta(1) \\ \cdot \\ \theta(n) \end{array} \right\}$$

```

clear all
global n Dn xx w t Tf
global Ve B;

% Define constants
r0=300;
v0=sqrt(398600.5/(6378.15+r0))*1000;    % initial velocity
Isp=300;
Ve=Isp*9.81/v0;
Tf=112.6

B=40900;    % Generic Spacecraft, B=(2*m0)/(r0*rho0*area*Cd)

n=25          % Number of LGL points
[Dn,xx,w]=diffmat(n);
t=(Tf/2)*(xx+1);

% There are linear periodic constraints; therefore need A
A=[1,zeros(1,n-2),-1,zeros(1,6*n);          % r(1)-r(n)=0
   zeros(1,1*n),1,zeros(1,n-2),-1,zeros(1,5*n); % v(1)-v(n)=0
   zeros(1,2*n),1,zeros(1,n-2),-1,zeros(1,4*n)]; % gamma(1)-gamma(n)=0

% Lower and upper limits for [r;v;gamma;m;T;eps;theta;A;c]
% r(1)=1, theta(1)=0

%           r           ;   v           ;   gamma           ;   mass           ;
l=[1;zeros(n-1,1);zeros(n,1); -(pi)*ones(n,1);1; zeros(n-1,1);...
   zeros(n,1);-pi*ones(n,1);zeros(n,1);0;0;0;zeros(5*n,1)];
%   thrust           ;   eps           ;   theta           ;   A           ; 5 c eqns

%           r           ;   v           ;   gamma           ;   mass           ;
u=[1;inf*ones(n-1,1);inf*ones(n,1); (pi)*ones(n,1);ones(n,1);...
   5*ones(n,1);pi*ones(n,1);0;inf*ones(n-1,1);0;0;0;zeros(5*n,1)];
%   thrust           ;   eps           ;   theta           ;   A           ; 5 c eqns

[xopt0] = optinitialfixed;
funobj = 'optobj';
funcon = 'optconfixed';
verifyLevel=0;
derivativeLevel=0;

[xopt,f,g,c,CJac,inform,lambda,iter,istate]=npsol(A,l,u,xopt0,funobj,funcon,verifyLevel,derivativeLevel);

r=xopt(1:n);          v=xopt(n+1:n*2);
gamma=xopt(2*n+1:n*3); m=xopt(3*n+1:n*4);
T=xopt(4*n+1:n*5);    eps=xopt(5*n+1:n*6);
theta=xopt(6*n+1:n*7);

```

Figure IV-1 *optmainfixed3.m* MATLAB script file

The next significant part of *optmainfixed3.m*, part II, sets the lower and upper limits (l and u) for each state, control, and constraint equation. For a free final time

problem, the lower and upper limits of the final time are also needed. The lower and upper limits on the states and controls are set to meet the constraints given in Chapter II and repeated here for clarity. Note that the limits at each LGL point must be specified. The radius initial value was set equal to one by setting both the lower and upper limit equal to one for $r(1)$. The rest of the limits on r and the other states were set as wide as possible. For instance, the velocity has lower limits of zero and upper limits of infinity. Basically, no limits at all. The constraints (A and c equations) are set equal to zero by specifying the lower AND upper limit as zero.

State constraints (r, v, γ, m, θ)

$$r(0) - r(t_f) = 0 \quad (\text{or } r(0) = r(t_f) = 1 \text{ for the pinned boundary condition})$$

$$v(0) - v(t_f) = 0$$

$$\gamma(0) - \gamma(t_f) = 0$$

$$\frac{-\pi}{2} \leq \gamma \leq \frac{\pi}{2}$$

$$0 \leq \bar{m} \leq 1 \quad (\text{normalized mass})$$

$$0 \leq \theta$$

Control Constraints (T, ε)

$$0 \leq \bar{T} \leq 5 \quad (\text{normalized thrust})$$

$$-\pi \leq \varepsilon \leq \pi$$

Part III contains the command line that actually calls the NPSOL software. Inputs include the A matrix, the lower and upper limits (l,u), the initial guess xopt0, the

objective function or cost (funobj), the constraint function (funcon), the verifylevel and derivativelevel.

Several outputs are also generated. These include the optimal state and control histories (xopt), the final value of the objective/cost (f), an array of the objective gradient (g), the final values of the nonlinear constraint functions (c) and the final values of the Jacobian matrix of the nonlinear constraints (CJac). The value "inform" reports the result of the call to NPSOL. An inform=0 is desirable and means that "the iterations have converged to a point that satisfies the optimality conditions". The term "iter" is the number of major iterations performed. The term "istate" describes the status of the constraints. [Ref. 10]

The output "lambda" is used to generate the costates. These costates are important in verifying the necessary conditions of optimality.

The five normalized state Equations (II-8 through II-12) are the five constraint equations ("c" equations) contained in *optconfixed.m* as shown in Figure IV-2. The first part of *optconfixed.m* is a simple exponential density model. Since *optconfixed.m* is called repeatedly, the density values change as the optimal radius history vector, r , is found by NPSOL. The constraint (or "c") equations are the nonlinear state equations in the form $\dot{x} - f = 0$ and formatted using the differential matrix Dn .

Each scalar constraint must be met at every point in time, therefore, it is written as a vector that contains the values of the constraint at each LGL point. As an example of the formulation, the r state equation (Equation II-14) is formatted as a constraint, and then written in the required format. Note that r , v , and γ are all $n \times 1$ vectors.

$$\dot{\bar{r}} = \bar{v} \cdot \sin(\gamma) \quad (\text{state equation}) \quad (\text{II-14})$$

$$\dot{\bar{r}} - \bar{v} \cdot \sin(\gamma) = 0 \quad (\text{constraint equation})$$

$$c(1:n,1) = (2/t_f) * (Dn * r) - (v * \sin(\gamma)); \quad (\text{formatted constraint equation})$$

```
function [c] = optconfixed(xopt)
% NPSOL Implementation of non-linear equations of motion and constraints
% Note, this only works for case where initial altitude is 300 km.
% Otherwise, you must change rinitial below.
global n Dn xx w t;
global B Ve Tf;
r =xopt(1:n);
v =xopt(n+1:n*2);
gamma =xopt(2*n+1:n*3);
m=xopt(3*n+1:n*4);
T=xopt(4*n+1:n*5);
eps=xopt(5*n+1:n*6);
theta=xopt(6*n+1:n*7);

% Calculate density for use in drag equations
% Changes density only when r is greater than specified
rho=ones(n,1); % initially assume normalized density =1 for all r
rinitial=6678.15;
j1=find(abs(r)>(rinitial-25)/rinitial); % returns indices where true
rho(j1)=1.87e-11*exp(-1*(r(j1)*rinitial-6678.15)/50.3)/(1.87e-11);
j1=find(abs(r)>(rinitial+25)/rinitial); % returns indices where true
rho(j1)=6.66e-12*exp(-1*(r(j1)*rinitial-6728.15)/54.8)/(1.87e-11);
j1=find(abs(r)>(rinitial+75)/rinitial); % returns indices where true
rho(j1)=(2.62e-12)*exp(-1*(r(j1)*rinitial-6778.15)/58.2)/(1.87e-11);
D=rho.*(v.^2);
t=(Tf/2)*(xx+1);
c(1:n,1)=(2/Tf)*(Dn*r)-(v.*sin(gamma));
c(1*n+1:n*2,1)=(2/Tf)*(Dn*v)-(-(1./r.^2).*(v.*sin(gamma)
+(T.*cos(eps)-D)./(m*B)));
c(2*n+1:n*3,1)=(2/Tf)*(Dn*gamma)-(((v.^2)./r
-(1./r.^2)).*(cos(gamma))./v + (T.*sin(eps))./(m.*v*B)));
c(3*n+1:n*4,1)=(2/Tf)*(Dn*m)-(-T./(Ve*B));
c(4*n+1:n*5,1)=(2/Tf)*(Dn*theta)-(v.*cos(gamma)./r);
```

Figure IV-2 Nonlinear Constraints File, *optconfixed.m*

The objective or cost function is incorporated into the file *optobj.m*. This file, as shown in Figure IV-3, simply creates the required function file for input into the NPSOL

command line in *optmainfixed3.m*. The input is the *xopt* vector and the output is the value of the cost (*objf*).

```
function [objf] = optobj(xopt)

% Created by Capt Larry Halbach, Naval Postgraduate School
% 3 Sep 99

global n Dn w

r =xopt(1:n);
v =xopt(n+1:n*2);
gamma =xopt(2*n+1:n*3);
m=xopt(3*n+1:n*4);
T=xopt(4*n+1:n*5);
eps=xopt(5*n+1:n*6);
theta=xopt(6*n+1:n*7);

objf = sum(w.*T)/2;
```

Figure IV-3 Cost Function File, *optobj.m*

One more file was used to create the initial guess. The initial guess can impact the results and therefore should be as good as possible. A function file called *optinitialfixed.m*, shown in Figure IV-4, was created to generate the initial guess based on the results of a previous run, typically at smaller *n*. If a previous run was not available, the following initial guesses were used.

<i>r0</i> =ones(<i>n</i> ,1)	<i>v0</i> =ones(<i>n</i> ,1)
<i>gamma0</i> =zeros(<i>n</i> ,1)	<i>m0</i> =(1-.0001*linspace(1,10, <i>n</i>))'
<i>T0</i> =5*ones(<i>n</i> ,1)	<i>eps0</i> =zeros(<i>n</i> ,1)
<i>theta0</i> =(linspace(0, <i>Tf0</i> , <i>n</i>))'	<i>Tf0</i> =112.6

```

function [xopt0] = optinitialfixed

% This function generates and returns the initial guess for optmain
% to run NPSOL. It splines the data from a run with lower n into
% a guess for a run with larger n. The filename in the load command
% must be changed to the appropriate name.
%
% Capt Lawrence Halbach, Naval Postgraduate School
% 13 Sep 99

global xx n

load jenNPSOLN20 t xopt;      % ensure correct filename and old value
old=20;                      % value of n from loaded filename
to=t;                        % simply renames the t vector
t=(Tf/2)*(xx+1);             % recreates the t vector, same as in main program

% Generate initial guesses

r0=spline(to,xopt(1:old),t);
v0=spline(to,xopt(old+1:2*old),t);
gamma0=spline(to,xopt(2*old+1:3*old),t);
m0=spline(to,xopt(3*old+1:4*old),t);
T0=spline(to,xopt(4*old+1:5*old),t);
eps0=spline(to,xopt(5*old+1:6*old),t);
theta0=spline(to,xopt(6*old+1:7*old),t);

clear xopt;

% Incorporate into initial guess column vector

xopt0=[r0;v0;gamma0;m0;T0;eps0;theta0];

```

Figure IV-4 Initial Guess Function, optinitial.m

B. RESULTS

1. Comparison to Jensen's Results

The state and control histories obtained using NPSOL as the NLP solver are presented in Figure IV-5 for $n=30$ and $t_f=112.6$. The results are compared to the results obtained by Jensen using *constr.m* as the solver for the same fixed final time of $t_f=112.6$ [Ref. 3].

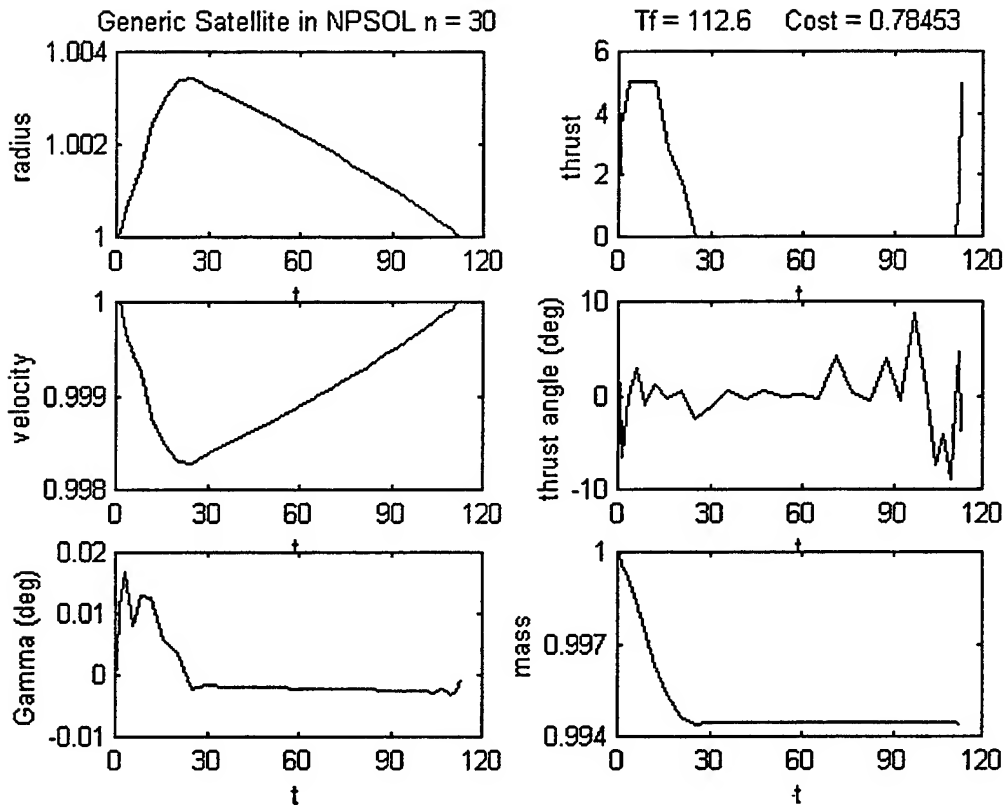


Figure IV-5 States and Controls using NPSOL Solver ($t_f=112.6$, $n=30$)

The radius increases to a maximum of 1.0034. This equates to an increase in altitude of 22.7 km over the original altitude of 300 km. The radius slowly returns back to the beginning altitude and completes this cycle in the specified $t_f=112.6$ time units. Jensen's results also peaked at 1.0034 with a similar profile. Note that the initial radius (at $t=0$) is fixed at 1.0 as discussed previously and shown by the code in Figure IV-1.

The velocity profiles were also similar. Both resemble an inverted radius profile and return to the original value at the required final time.

The flight path angle (γ) is nearly zero throughout the entire time period. This indicates that the orbit remains nearly circular. Note that the units in the plot are degrees. In radians, the change in γ is a barely discernable 0.00024.

The mass profile is a direct result of the thrust profile. When thrusting, the mass rate of decrease is directly proportional to the thrust as given by the state Equation II-9. When not thrusting, the mass remains constant. The final mass of the spacecraft, 0.9942, is a 0.58 percent decrease from the mass at the beginning of the maneuver.

The thrust profile behaves in "bang-bang" mode. This result was not found by Jensen using MATLAB's *constr.m* file. Jensen concludes that the thrust profile is "a smooth, continuous throttle burn." [Ref. 3] Under bang-bang control, the thrust will either be zero or maximum. In Figure IV-5, the thrust increases quickly to maximum thrust ($T_{\max}=5$), decreases very quickly to zero and remains zero until near the end. The final thrusting at the very end of the time period is also at T_{\max} . This thrusting is apparently used to circularize the orbit and meet the final time conditions. The impact of this final thrusting is particularly visible in the plot of the flight path angle. Further analysis on the thrust profile is conducted in Chapter VI.

The thrust angle shows little variation during thrusting. In Figure IV-5, the thrust angle quickly goes to near zero as the thrust increases to T_{\max} and then remains near zero. The thrust angle appears to change randomly during periods when the thrust is zero. This is a numerical issue since the steering is physically irrelevant when the thrust is zero.

The cost, as given by Equation II-20, is a ratio relating the amount of propellant used by the minimizing trajectory to the amount of propellant used by an FKT performed

at the original altitude. A cost of less than one indicates that this profile is more efficient, i.e. uses less propellant, than a low FKT maneuver for the same period.

The profile in Figure IV-5 yields significant savings over a low-FKT and agrees well with the findings by Jensen. For this scenario, the cost equaled 0.78453. This is a savings of 21.5 percent over an FKT performed at the original altitude. Jensen obtained a cost of 0.7837 which is a difference of 1/10th of one percent.

2. Effect of Final Time Constraint

The chosen final time greatly affects the cost index. The longer the period, the less the cost. Figure IV-6 shows how the costs vary with final time. This clearly shows the expected result that the cost, a ratio of the cost of the periodic reboost to the cost of a low-FKT, decreases with a longer period.

For example, the cost of 0.39729 for the $t_f = 700$ case is much less than for the shorter period discussed above. The longer period yields a higher maximum altitude from which it takes longer to descend. At the higher altitude, velocities are less and the densities are much less. The minimum density experienced at the maximum radius in Figure IV-5 is 0.2622 which equates to $4.9031\text{e-}12 \text{ kg/m}^3$. The minimum density for the $t_f = 700$ case is 0.1915 which equates to $3.5811\text{e-}12 \text{ kg/m}^3$ for this analysis. These factors decrease the cost by nearly 50 percent compared to the $t_f = 112.6$ case and by over 60 percent compared to a low altitude FKT.

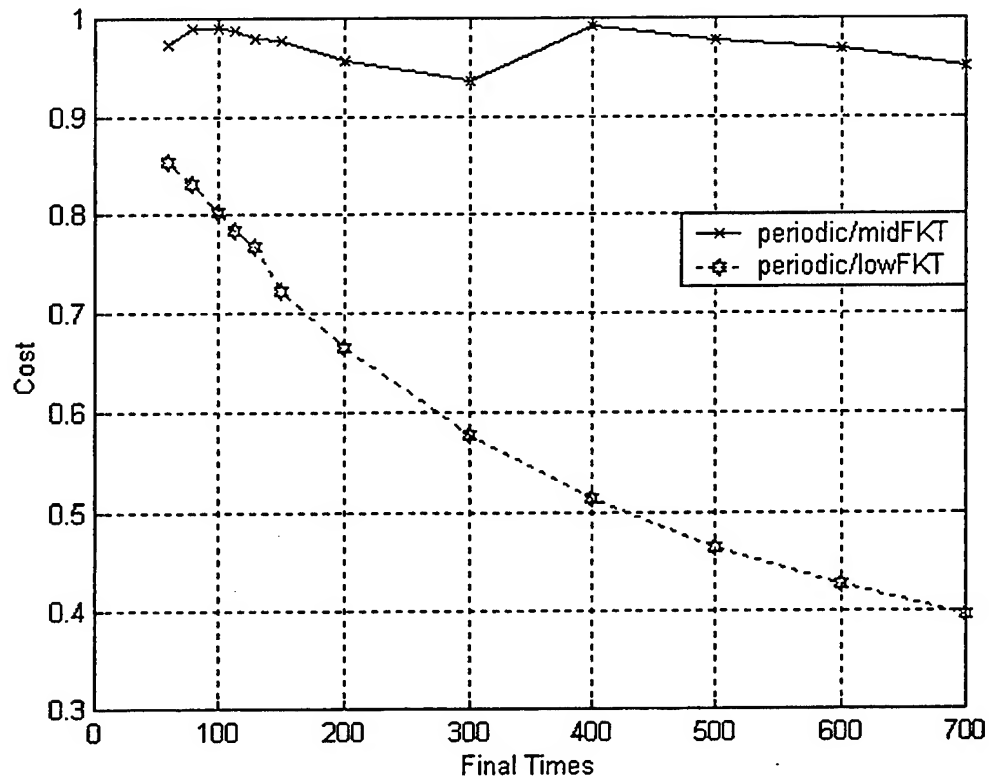


Figure IV-6 Periodic Reboost Cost Comparison

These trajectories were then compared to a Hohmann transfer, which traditionally is thought to be the most efficient transfer method. As described in Chapter II, a mid-FKT is similar in performance to a Hohmann transfer [Ref 1]. Therefore, the cost ratio of the periodic reboost method to the mid-FKT is almost the same as the cost ratio to a Hohmann transfer.

By dividing the periodic cost ratio plotted above by the mid-FKT cost ratio, a new measure of cost was obtained which is the ratio of the periodic reboost to the mid-FKT. Similar to the above analysis, a ratio less than one means that the periodic reboost has

lower costs. The following paragraph describes by example how the ratios were obtained for the case of $n=30$ and $t_f=112.6$.

From Figure IV-5, the middle altitude was determined to be 1.0017 which is halfway between the initial radius ($r=1$) and the highest radius ($r=1.0034$). The normalized atmospheric density at $r=1.0017$ is 0.7980 and the FKT velocity is 0.9983 ($=\sqrt{1/r}$). This creates a drag, D , at this altitude of 0.7953. By FKT definition, the thrust equals the drag. When the thrust is set equal to this value at all of the LGL points, the cost was determined to be 0.7953 with respect to a low-FKT as shown by

$$\text{FKT Cost} = \frac{1}{t_f} \int_0^{t_f} T dt = \frac{D}{t_f} \int_0^{t_f} dt = D$$

The ratio of the periodic reboost to the low-FKT was 0.78453. Therefore, the ratio of the periodic reboost to the mid-FKT is $0.78453/0.7953$ which equals 0.9865 for $t_f = 112.6$. Since this is less than one, it appears the periodic reboost is more efficient than the mid-FKT. Table IV-1 and Figure IV-6 contain the results from runs conducted with varying final time (t_f). The mid-FKT cost was recomputed for each run as described above for $t_f = 112.6$. As stated above, the cost of a mid-FKT is comparable to a Hohmann transfer. Therefore, the periodic reboost appears to be more efficient than the mid-FKT and the Hohmann.

Table IV-1 Mid-FKT Cost Analysis

Final Time	<u>Periodic Reboost</u> Low-FKT	<u>Mid-FKT</u> Low-FKT	<u>Periodic Reboost</u> Mid-FKT
112.6	0.78453	0.7948	0.987
130	0.7688	0.7843	0.980
150	0.72328	0.7396	0.978
200	0.66194	0.6861	0.965
300	0.57618	0.6148	0.937
400	0.51336	0.5177	0.992
500	0.46492	0.4757	0.977
600	0.42718	0.4412	0.968
700	0.3954	0.4174	0.947

Analysis for periods less than 112.6 yielded suspect profiles in which the state and control histories are not entirely reasonable. As an example, the states and controls for $t_f = 80$ show erratic behavior as shown in Figure IV-7. The radius and velocity histories have unrealistic spikes near the beginning and the end. Therefore, these cases are not included in the analysis.

Interestingly, the plot of the mid-FKT cost comparison in Figure IV-6 shows a local minimum near a final time of 300. A time free analysis was performed to examine this possibility.

The free final time run had the final time limited to between 100 and 400. A local minimum would result in a final time less than 400. In this case, the final time increased to the maximum limit of 400. The cost of 0.51398 is nearly identical to the cost (0.51336) obtained from the fixed final time run of $t_f = 400$. The mid-FKT/low-FKT cost ratio, calculated as above, equaled 0.5191 which yields a cost index of 0.990. The free

final time results agree well with the fixed final time results for $t_f=400$. Based on this analysis, a local minimum at 300 is unlikely.

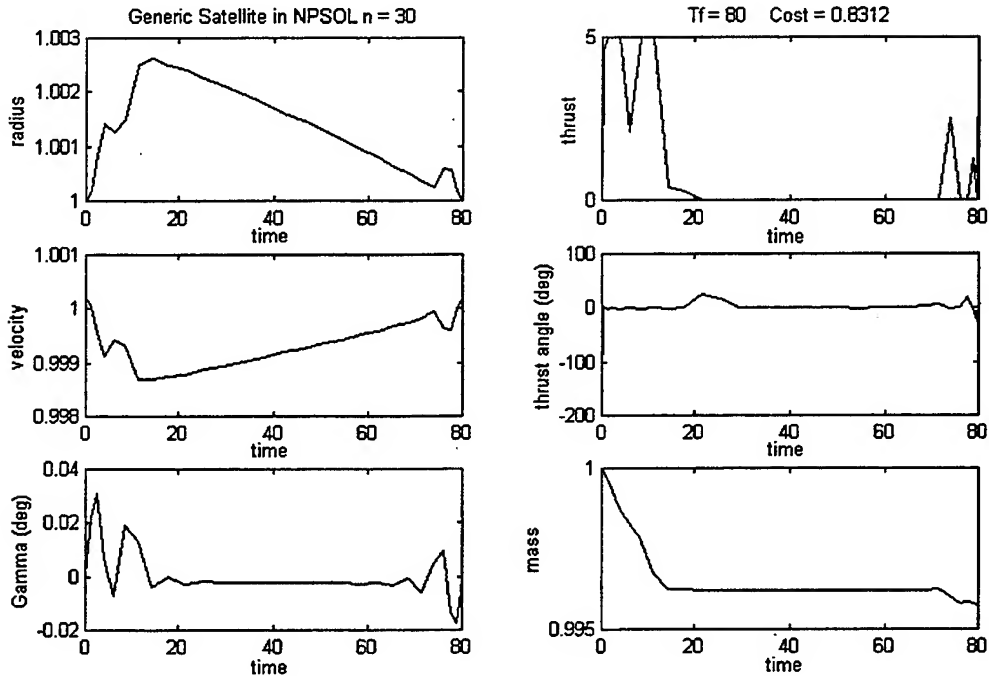


Figure IV-7 State and Control History, $t_f=80$

3. Effect of Radius Constraint

Many spacecraft are operated within an operational orbital belt that places both an upper and lower altitude restriction on the orbit. This prevents complete implementation of the optimal periodic reboost. Consider the case of $t_f=700$. The unconstrained maximum altitude is 1.0123. Setting the upper radius limit to 1.008 (equivalent to 53.4 km) ensured a bounded constraint. The results are presented in Figure IV-8.

The profile begins the same way as the unconstrained case with maximum thrust and rapid increase in radius. But, when the upper limit is reached, the thrust decreases and the radius flattens out until much later when it begins the familiar decay due to drag

back to the original altitude to meet the final time requirement. While maintaining the maximum allowed altitude, the spacecraft is flying an FKT trajectory, since at the maximum altitude, $r=1.008$, and $v = \sqrt{\frac{1}{r}} = 0.99602$. Thrust stabilizes at normalized thrust equal to normalized drag as given by

$$\bar{D} = \rho v^2 = 0.33457 * .99602^2 = .3319$$

At the original altitude, an FKT trajectory would require $T=1$. But at the higher altitude with its lower velocity and lower density, the required thrust is much less. This profile results in a higher cost than the unlimited altitude case: 0.44157 vice 0.39729.

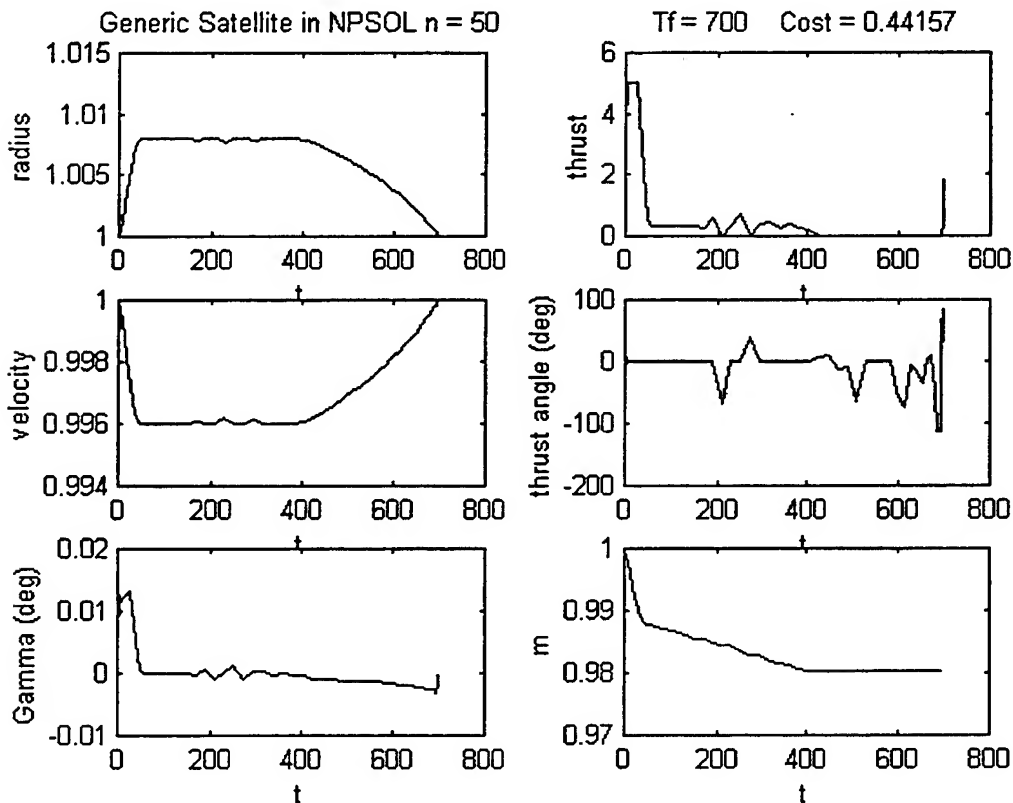


Figure IV-8 States and Controls for Altitude Limited Case ($t_f=700$, $n=50$)

4. Costates and Necessary Conditions

In this section, the outputs from the direct method analysis are checked against the necessary optimality conditions.

The necessary conditions for optimality, as described in Chapter II are

$$\text{Costates: } \dot{\lambda}^T = -\frac{\partial H}{\partial \mathbf{x}} \quad (\text{II-1})$$

$$\text{Optimality: } \frac{\partial H}{\partial \mathbf{u}} = 0 \quad (\text{II-2})$$

$$\text{and } \frac{\partial^2 H}{\partial \mathbf{u}^2} \geq 0 \quad (\text{II-3})$$

$$\text{Transversality I: } \lambda(t_f) = \frac{\partial M}{\partial \mathbf{x}_f} + \left(\frac{\partial \psi}{\partial \mathbf{x}_f} \right)^T \mathbf{v}_f \quad (\text{II-4})$$

Transversality II: (if final time free)

$$H(t_f) + \frac{\partial M(t_f)}{\partial t_f} + \mathbf{v}_f^T \frac{\partial \psi(t_f)}{\partial t_f} = 0 \quad (\text{II-5})$$

where,

$$H \equiv \text{the augmented Hamiltonian} = L + \lambda^T \mathbf{f} + \mu^T \mathbf{g}$$

in which $\dot{\mathbf{x}} = \mathbf{f}$ from the state equations and \mathbf{g} is the control inequality vector

given by

$$\mathbf{g} = \begin{Bmatrix} g_1 \\ g_2 \\ g_3 \\ g_4 \end{Bmatrix} = \begin{Bmatrix} T - T_{\max} \\ -T \\ \varepsilon - \pi \\ -\varepsilon - \pi \end{Bmatrix} \leq \begin{Bmatrix} 0 \\ 0 \\ 0 \\ 0 \end{Bmatrix}$$

$\mu^T g$ has the relation that $\mu \geq 0$ when $g = 0$

and $\mu = 0$ when $g < 0$

Since g_3 and g_4 are always less than zero, then $\mu_3 = 0$ and $\mu_4 = 0$.

Therefore, $\mu^T = \begin{Bmatrix} \mu_1 \\ \mu_2 \end{Bmatrix}$

The cost was given in Chapter II as

$$J = \frac{1}{t_f} \int_0^{t_f} \bar{T} dt$$

Also, $\lambda \equiv$ column vector of costates $= \begin{Bmatrix} \lambda_r \\ \lambda_v \\ \lambda_\gamma \\ \lambda_m \\ \lambda_\theta \end{Bmatrix},$

$\psi(t_f) \equiv$ final conditions,

$u \equiv$ vector of controls $= \begin{Bmatrix} T \\ \varepsilon \end{Bmatrix},$

and $x \equiv$ vector of states $= \begin{Bmatrix} r \\ v \\ \gamma \\ m \\ \theta \end{Bmatrix}$

The first part of the MATLAB script file *optfixresults.m*, takes the NPSOL output "lambda" and generates the costates related to the state equations by using the equation

$$\lambda(t_i) = \frac{\lambda_{NLP}}{w_i} \quad (IV-1)$$

where w_i are the weights at the LGL points. [Ref. 4]

The vector lambda from NPSOL contains additional values, besides the costates. The first $7*n$ values (n =number of LGL points) contain the lambdas associated with the n initial conditions on each state (r,v,γ,m,θ) and each control (T,ϵ) in the following order: ($r,v,\gamma,m,T,\epsilon,\theta$). The next three components, $\text{lambda}(7*n+1)$ to $\text{lambda}(7*n+3)$, correspond to the linear constraints. The next $5*n$ elements contain the costates for the five state equations for (r,v,γ,m,θ). These are the values of interest for analysis of the necessary conditions given above.

The code to accomplish this in the MATLAB file is given in Figure IV-9.

```
lamr=lambda(7*n+4:8*n+3)./(w*(Tf/2));
lamv=lambda(8*n+4:9*n+3)./(w*(Tf/2));
lamgamma=lambda(9*n+4:10*n+3)./(w*(Tf/2));
lammass=lambda(10*n+4:11*n+3)./(w*(Tf/2));
lamtheta=lambda(11*n+4:12*n+3)./(w*(Tf/2));
```

Figure IV-9 Costates Generation Code

These costates were then plotted against time. Figure IV-10 shows the plots for the results of a run at $t_f=112.6$ and $n=30$. The costates obtained from this analysis were noisy. A digital filter designed by T. P. Thorvaldsen and based on the research of Ross, Fahroo, and Thorvaldsen was applied to smoothen the costates. The filtered costates are presented in Figure IV-11 and are used in the following analysis. The filtered costates contrast sharply with the unfiltered costates. The large cyclic changes in magnitude are

removed and the large spikes near the beginning and end of the time period are greatly reduced, though still visible

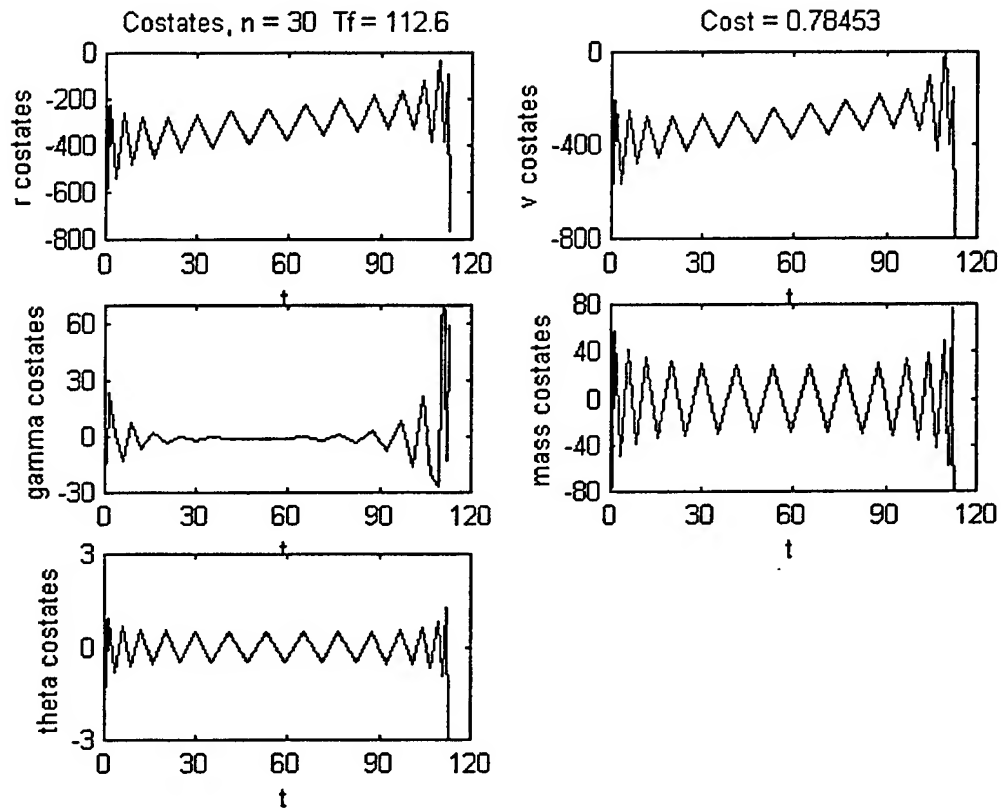


Figure IV-10 Plots of Costates ($n=30$, $t_f=112.6$)

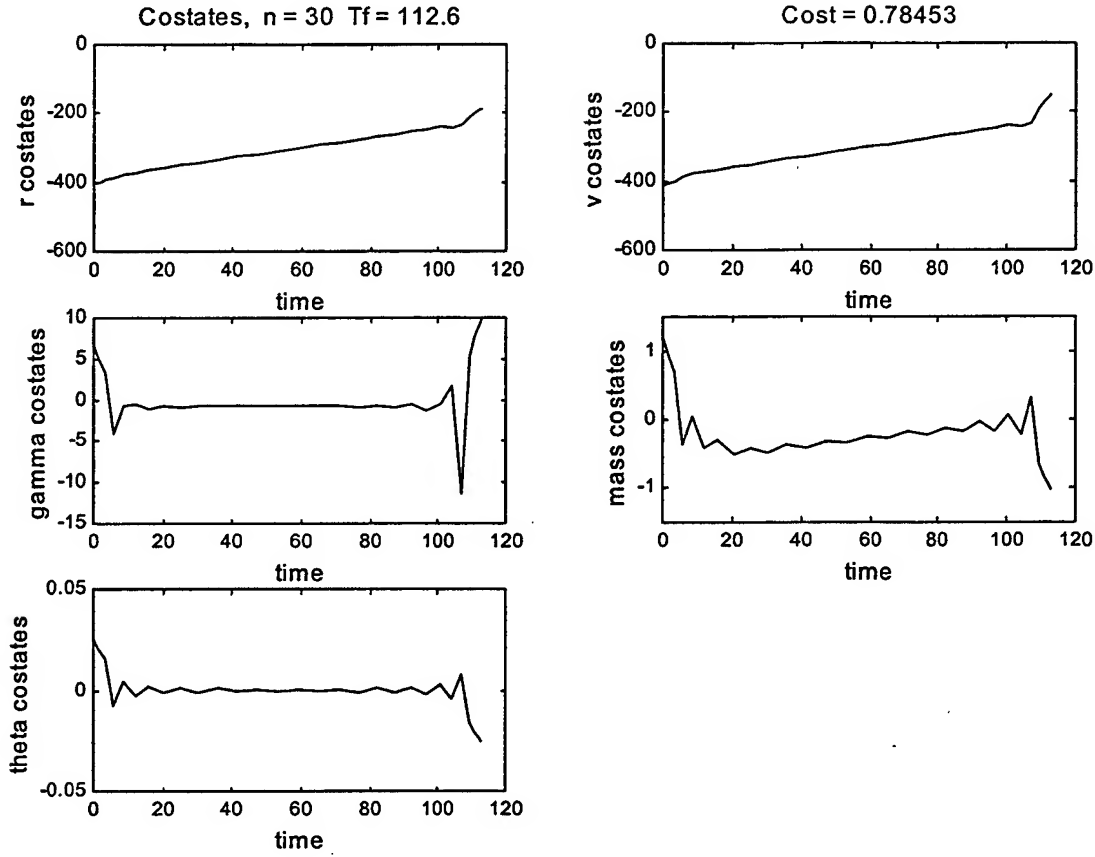


Figure IV-11 Filtered Costates for n=30

An analysis was performed using these filtered costate estimates. The analysis begins with the Hamiltonian, which is given as:

$$H \equiv \text{Hamiltonian} = L + \lambda^T \mathbf{f} + \mu^T \mathbf{g}$$

$$H = \frac{T}{t_f} + [\lambda_r \quad \lambda_v \quad \lambda_\gamma \quad \lambda_m \quad \lambda_\theta] \cdot [\mathbf{f}] + [\mu_1 \quad \mu_2] \cdot \begin{bmatrix} g_1 \\ g_2 \end{bmatrix} \quad (\text{IV-2})$$

$$H = \frac{T}{t_f} + \lambda_r v \sin \gamma + \lambda_v \left(\frac{-\sin \gamma}{r^2} + \frac{T \cos \varepsilon - D}{mB} \right) + \lambda_\gamma \left[\left(\frac{v^2}{r} - \frac{1}{r^2} \right) \frac{\cos \gamma}{v} + \frac{T \sin \varepsilon}{mvB} \right] - \frac{\lambda_m T}{v_e B} + \lambda_\theta \frac{v \cos \gamma}{r} + \mu_1 (T - T_{\max}) + \mu_2 (-T)$$

Note: All of the values used in these equations are the normalized values. The bar over the symbol is not included for clarity of presentation.

The PMP states that the Hamiltonian, H , is a minimum at the optimal control u^* .

This applies at every point in the trajectory.

The optimality conditions for the controls are given by

$$\frac{\partial H}{\partial u} = 0 \quad (IV-3)$$

$$\frac{\partial H}{\partial u} = \left[\frac{\partial H}{\partial T} \quad \frac{\partial H}{\partial \varepsilon} \right] = [0 \quad 0] \quad (IV-4)$$

$$\frac{\partial H}{\partial T} = \frac{1}{t_f} + \lambda_v \frac{\cos \varepsilon}{mB} + \lambda_\gamma \frac{\sin \varepsilon}{mvB} - \lambda_m \left(\frac{1}{v_e B} \right) + \mu_1 - \mu_2 = 0 \quad (IV-5)$$

$$\frac{\partial H}{\partial \varepsilon} = -\lambda_v \frac{T \sin \varepsilon}{mB} + \lambda_\gamma \frac{T \cos \varepsilon}{mvB} = 0 \quad (IV-6)$$

In $\frac{\partial H}{\partial T}$, μ_1 equals zero except where the thrust, T , equals T_{\max} and μ_2 equals zero

everywhere except where $T=0$. The thrust should change from T_{\max} to $T=0$ or vice versa whenever the switching function, S , changes sign, where S is given by

$$S = \frac{1}{t_f} + \lambda_v \frac{\cos \varepsilon}{mB} + \lambda_\gamma \frac{\sin \varepsilon}{mvB} - \lambda_m \left(\frac{1}{v_e B} \right) \quad (IV-7)$$

To check this condition, the switching function and thrust profile, scaled to $1/1000^{\text{th}}$, are plotted together against time. In Figure IV-12, the original thrust profile

from Figure IV-5 is plotted with the switching function that results from the unfiltered costates. As can be seen, as the switching function crosses from negative to positive near time 15, the thrust drops to zero. Later, the switching function becomes negative for a moment and the thrusting increases (to T_{\max}). It appears the solution obeys the switching function given by Equation IV-7.

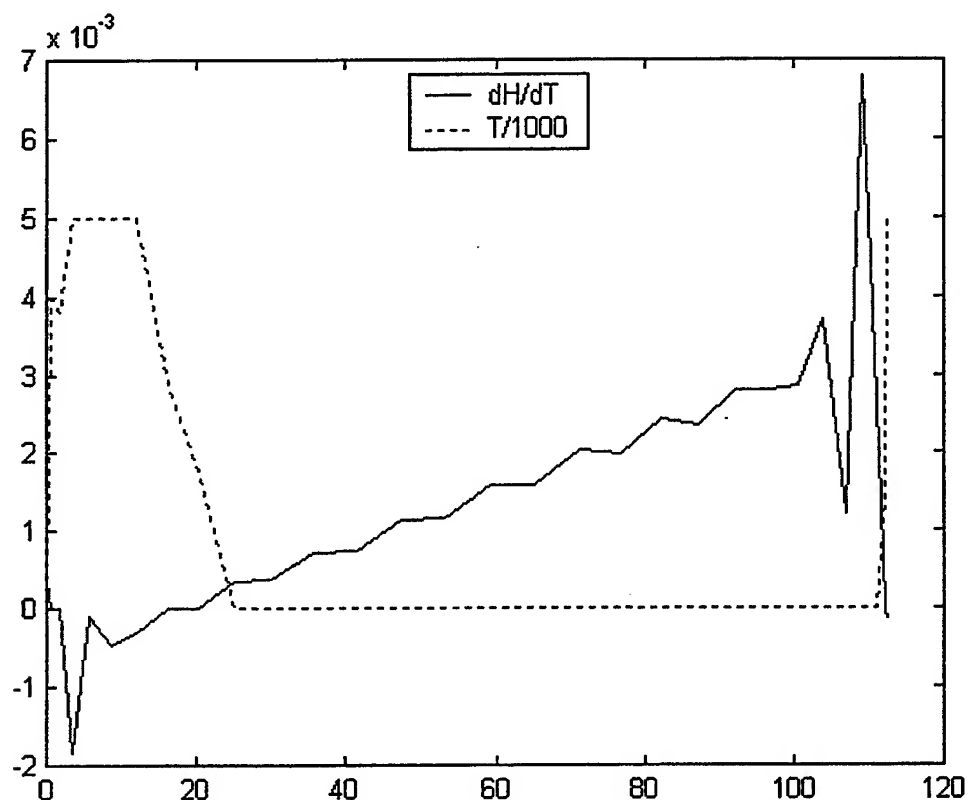


Figure IV-12 Switching Condition, S, and Thrust/1000

In Figure IV-13, the filtered costates are used to generate the switching function. Based on this switching function, the thrust profile was determined and is also plotted in Figure IV-13. The filtered costates yield a switching function that leads to a bang-bang thrust profile. The thrust is a maximum when the switch is negative and goes to zero

when the switch becomes positive. The switching function is discussed further in Chapter VI.

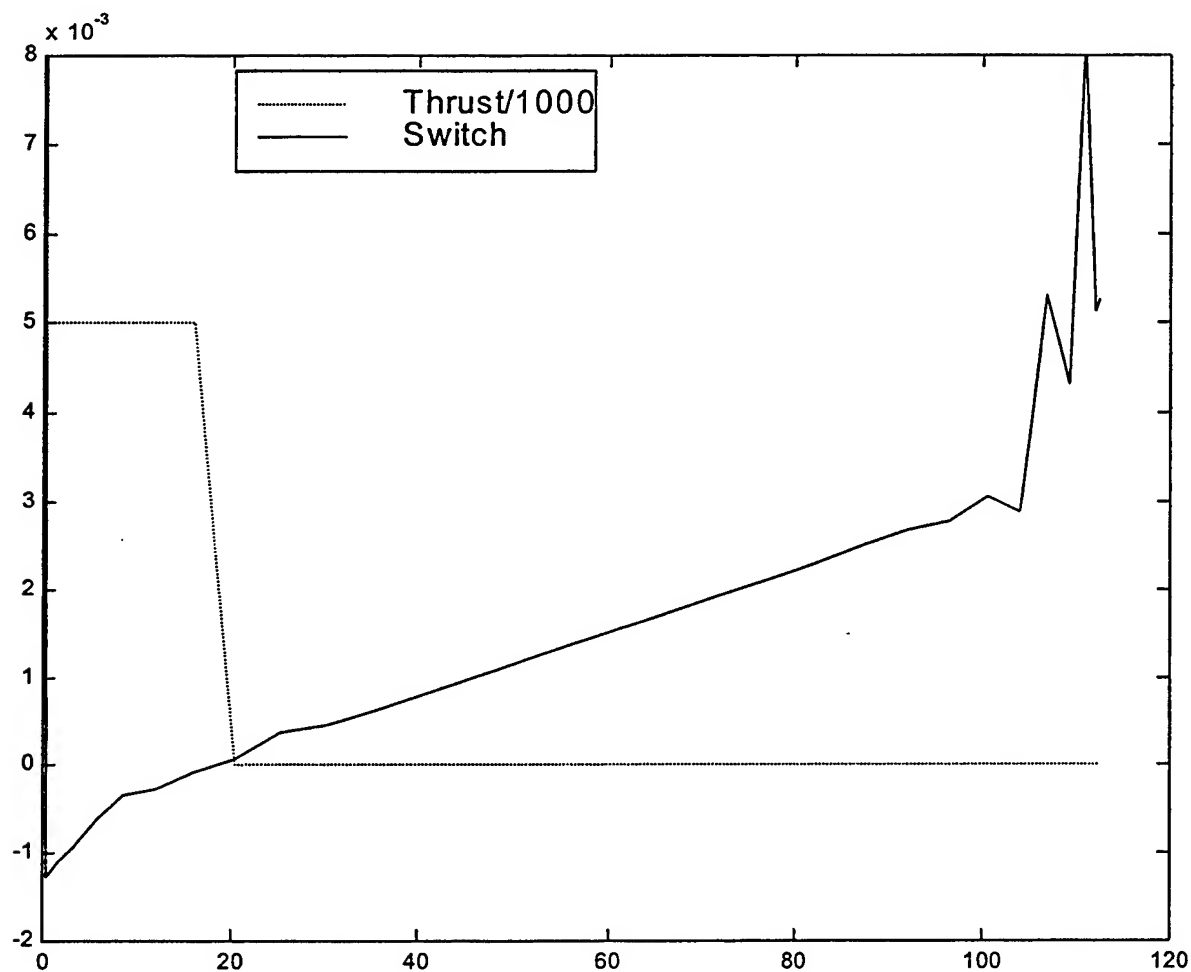


Figure IV-13 Switch and Thrust Using Filtered Costates

Figure IV-14 contains the graph of the other optimality condition, $\frac{\partial H}{\partial \varepsilon}$. According to Equation IV-6, this should equal zero at all times. The results generally agree with this requirement except for large errors at the beginning and final times. The

cause of these errors is unknown, but the deviations occur in every plot of the costates and necessary conditions. Overall, the optimality conditions appear to be met.

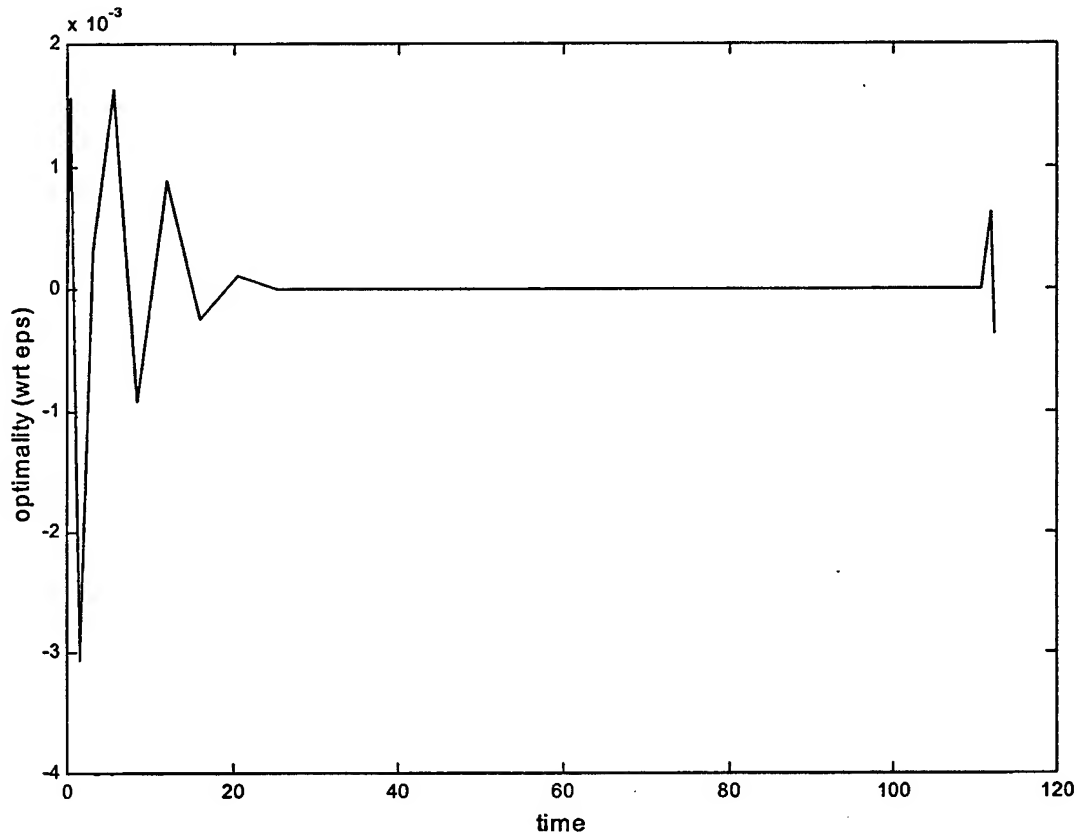


Figure IV-14 Optimality Condition, $\frac{\partial H}{\partial \varepsilon} = 0$

The second partial of the Hamiltonian with respect to the unconstrained controls,

$\frac{\partial^2 H}{\partial u^2} \geq 0$, is also an important tenet of PMP. Since thrust is constrained, only the second

partial with respect to the thrust angle is analyzed and is given by

$$\frac{\partial^2 H}{\partial \varepsilon^2} = -\lambda_v \frac{T \cos \varepsilon}{mB} - \lambda_\gamma \frac{T \sin \varepsilon}{mvB} \quad (IV-8)$$

Figure IV-15 provides a plot of $\frac{\partial^2 H}{\partial \varepsilon^2}$. It appears that the steering angle does meet the requirement that $\frac{\partial^2 H}{\partial \varepsilon^2} \geq 0$.

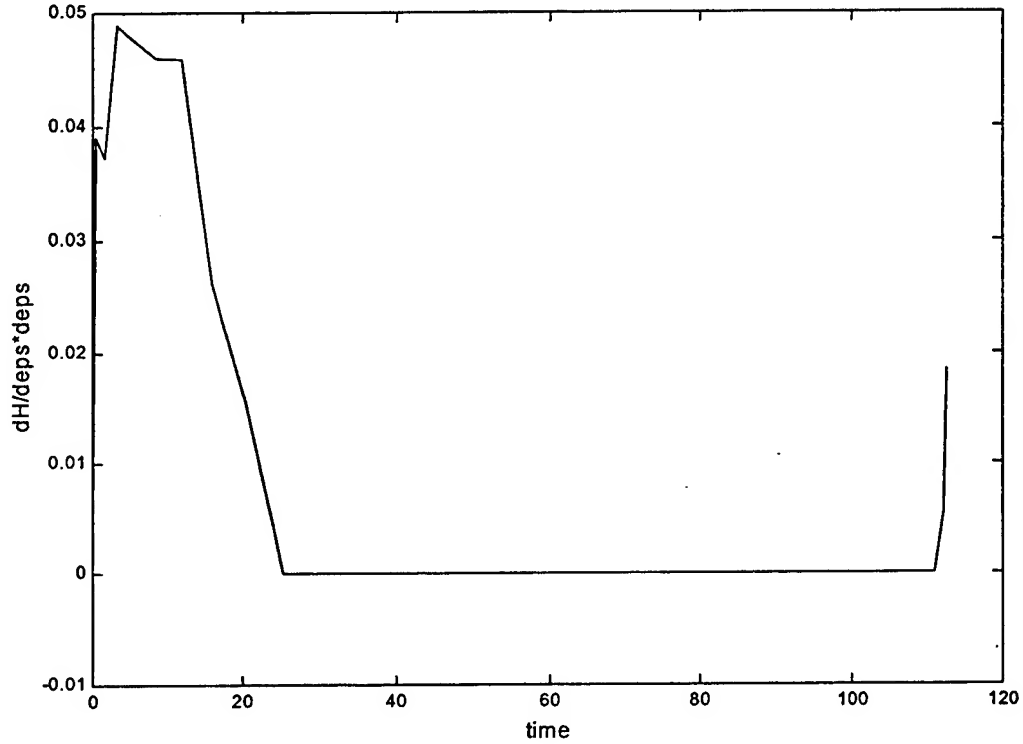


Figure IV-15 Plot of $\frac{\partial^2 H}{\partial \varepsilon^2}$

The Hamiltonian, H , should be zero for optimality. Figure IV-16 contains a plot of H as given by

$$H = \frac{T}{t_f} + \lambda_r v \sin \gamma + \lambda_v \left(\frac{-\sin \gamma}{r^2} + \frac{T \cos \varepsilon - D}{mB} \right) + \lambda_\gamma \left[\left(\frac{v^2}{r} - \frac{1}{r^2} \right) \frac{\cos \gamma}{v} + \frac{T \sin \varepsilon}{mvB} \right] - \frac{\lambda_m T}{v_e B} + \lambda_\theta \frac{v \cos \gamma}{r}$$

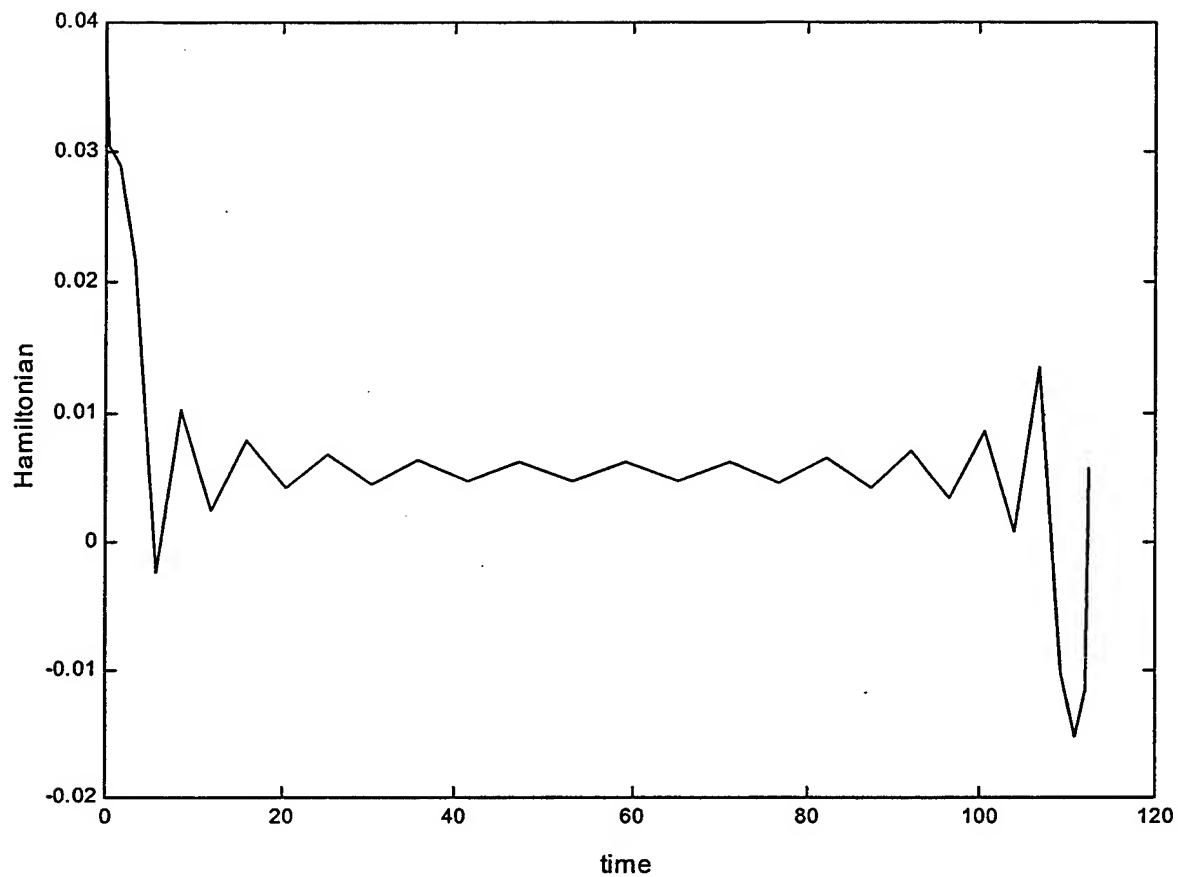


Figure IV-16 Plot of Hamiltonian

As shown in Figure IV-16, the Hamiltonian is nearly constant at $H=0$ except at the beginning and the end.

The necessary conditions for the costates are given by Equation II-1 which can be rewritten as

$$\dot{\lambda}^T + \frac{\partial H}{\partial x} = 0 \quad (\text{IV-9})$$

The individual components become

$$\dot{\lambda}_r + \frac{\partial H}{\partial r} = \dot{\lambda}_r + \lambda_v \frac{2 \sin \gamma}{r^3} - \lambda_\gamma \left(\frac{v^2}{r^2} - \frac{2}{r^3} \right) \frac{\cos \gamma}{v} - \lambda_\theta \frac{v \cos \gamma}{r^2} \quad (\text{IV-10})$$

$$\dot{\lambda}_v + \frac{\partial H}{\partial v} = \dot{\lambda}_v + \lambda_r \sin \gamma - \frac{2 \lambda_v \rho v}{mB} + \lambda_\gamma \left[\left(\frac{1}{r} + \frac{1}{r^2 v^2} \right) \cos \gamma - \frac{T \sin \varepsilon}{m v^2 B} \right] + \lambda_\theta \frac{\cos \gamma}{r} \quad (\text{IV-11})$$

$$\dot{\lambda}_\gamma + \frac{\partial H}{\partial \gamma} = \dot{\lambda}_\gamma + \lambda_r v \cos \gamma - \lambda_v \frac{\cos \gamma}{r^2} - \lambda_\gamma \left(\frac{v^2}{r} - \frac{1}{r^2} \right) \frac{\sin \gamma}{v} - \lambda_\theta \frac{v \sin \gamma}{r} \quad (\text{IV-12})$$

$$\dot{\lambda}_m + \frac{\partial H}{\partial m} = \dot{\lambda}_m - \lambda_v \left(\frac{T \cos \varepsilon - D}{m^2 B} \right) - \lambda_\gamma \frac{T \sin \varepsilon}{m^2 v B} \quad (\text{IV-13})$$

$$\dot{\lambda}_\theta + \frac{\partial H}{\partial \theta} = \dot{\lambda}_\theta \quad (\text{IV-14})$$

In order to evaluate these expressions, the values of $\dot{\lambda}$ must first be computed. This was done using the differential matrix introduced earlier. The formulation is given by

$$\dot{\lambda} = \begin{pmatrix} 2 \\ t_f \end{pmatrix} (D_n * \lambda) \quad (\text{IV-15})$$

The costate necessary conditions were then plotted in Figure IV-17 based on Equations IV-10 to IV-14. The plots should equal zero if the results match the theory. In general, these plots do meet the requirements fairly well except for λ_r and at the beginning and end of each plot.

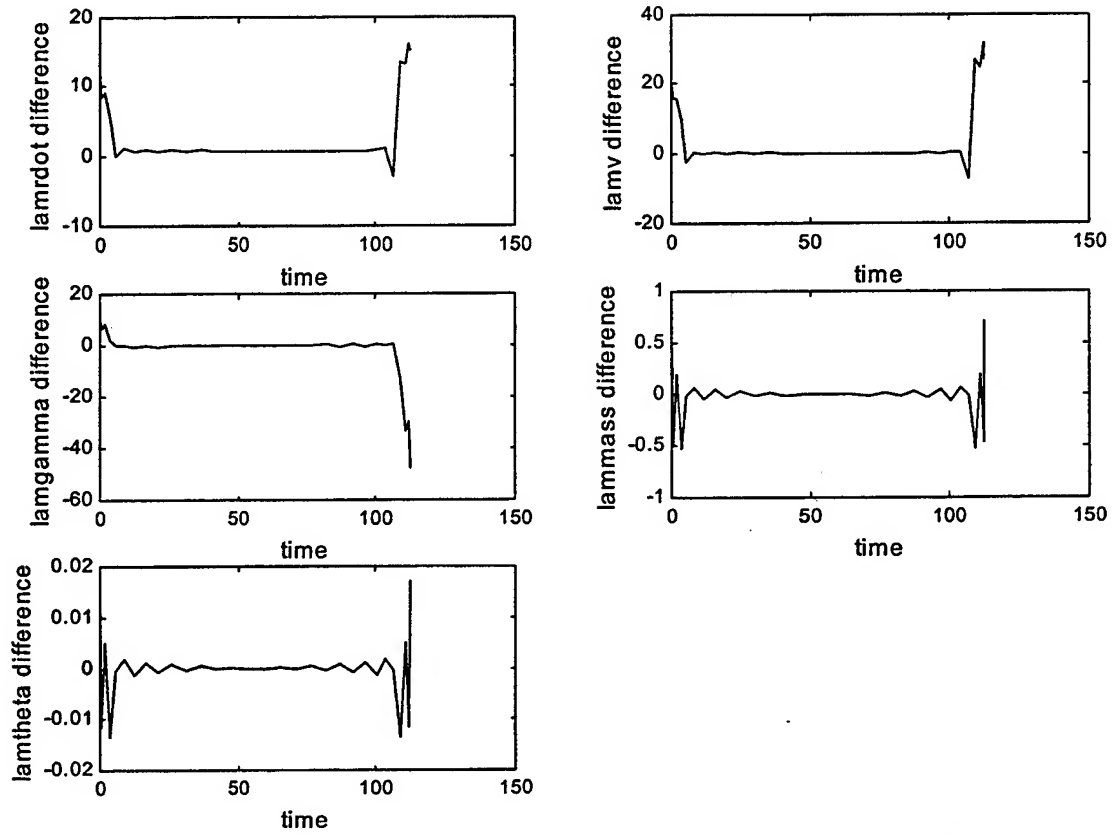


Figure IV-17 Costate Difference Plots, $\dot{\lambda}^T + \frac{\partial H}{\partial x} = 0$

The transversality condition is a function of any final time cost elements, $M(t_f)$, and the final time conditions, $\psi(t_f)$. In this problem, the cost function is an integral function and does not have a final time cost element, so $M(t_f) = 0$. Therefore

$\frac{\partial M(t_f)}{\partial x} = 0$, which results in the transversality condition

$$\lambda^T(t_f) = \frac{\partial M(t_f)}{\partial x} + v^T \frac{\partial \psi(t_f)}{\partial x} = v^T \frac{\partial \psi(t_f)}{\partial x} \quad (IV-16)$$

In this problem, the final conditions are as given by

$$\psi(t_f) = \begin{Bmatrix} r(t_f) - r(0) \\ v(t_f) - v(0) \\ \gamma(t_f) - \gamma(0) \end{Bmatrix} \quad (\text{IV-17})$$

The partial derivative with respect to the states is given by

$$\frac{\partial \psi(t_f)}{\partial \mathbf{x}} = \begin{bmatrix} \frac{\partial(r(t_f)-1)}{\partial r} & \frac{\partial(r(t_f)-1)}{\partial v} & \frac{\partial(r(t_f)-1)}{\partial \gamma} & 0 & 0 \\ \frac{\partial(v(t_f)-1)}{\partial r} & \frac{\partial(v(t_f)-1)}{\partial v} & \frac{\partial(v(t_f)-1)}{\partial \gamma} & 0 & 0 \\ \frac{\partial(\gamma(t_f)-\gamma(0))}{\partial r} & \frac{\partial(\gamma(t_f)-\gamma(0))}{\partial v} & \frac{\partial(\gamma(t_f)-\gamma(0))}{\partial \gamma} & 0 & 0 \end{bmatrix} \quad (\text{IV-18})$$

which becomes:

$$\frac{\partial \psi(t_f)}{\partial \mathbf{x}} = \begin{bmatrix} 1 & 0 & 0 & 0 & 0 \\ 0 & 1 & 0 & 0 & 0 \\ 0 & 0 & 1 & 0 & 0 \end{bmatrix}$$

The resulting transversality equation is then

$$\lambda^T(t_f) = [\nu_r \quad \nu_v \quad \nu_\gamma] \cdot \begin{bmatrix} 1 & 0 & 0 & 0 & 0 \\ 0 & 1 & 0 & 0 & 0 \\ 0 & 0 & 1 & 0 & 0 \end{bmatrix}$$

$$\lambda^T(t_f) = [\nu_r \quad \nu_v \quad \nu_\gamma \quad 0 \quad 0]$$

or separated into components, the transversality condition is:

$$\begin{aligned} \lambda_r(t_f) &= \nu_r \\ \lambda_v(t_f) &= \nu_v \\ \lambda_\gamma(t_f) &= \nu_\gamma \\ \lambda_m(t_f) &= 0 \\ \lambda_\theta(t_f) &= 0 \end{aligned} \quad (\text{IV-19})$$

C. NUMERICAL ANALYSIS ISSUES

1. Effects of Problem Formulation

The formatting in the "main.m" file, such as in *optmainfixed3.m*, impacted the solutions. Several cases were run in which the linear constraint matrix, A, and the lower and upper bounds, l and u, were defined differently than described above. Instead of including the $r(1)-r(n)=0$ and $v(1)-v(n)=0$ constraints into the A matrix, their lower and upper bounds of $r(1)$, $r(n)$, $v(1)$, and $v(n)$ were set equal to 1 in both the lower and upper bounds. This forced these to be equal, thus forcing $r(1)=r(n)=1$ and $v(1)=v(n)=1$. This formulation differs from the original formulation in which $r(1)=r(n)=1$ but the velocity terms had a lower bound of zero and no upper bound. (See part II of Figure IV-1) Throughout this chapter, the radius plots have initial and final normalized radii that are forced to equal one ($r(1)=r(n)=1$).

The new formulation changed the results. The case of $n=30$, $t_f=112.6$ is given in Figure IV-18 to demonstrate. The difference in cost is immediately noticeable. While the originally formatted problem gave a cost of 0.78453, this formulation yielded a higher cost of 0.79767.

Since cost is a function of thrust, the thrust profiles were overlaid in Figure IV-19 to look for differences. The thrust profile labeled as "original" is the thrust profile obtained from the proper formulation already presented during the results discussion. The profile labeled as "modified" represents the formulation being discussed here. The profiles are generally alike, but differences do exist.

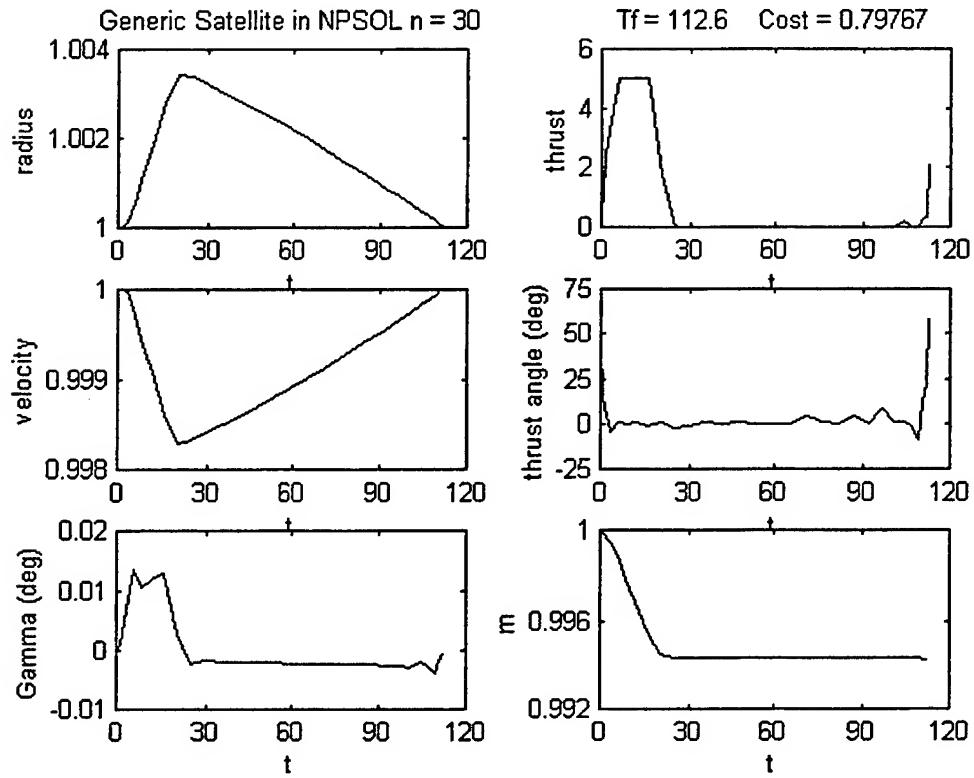


Figure IV-18 Results from Modified Problem Formulation

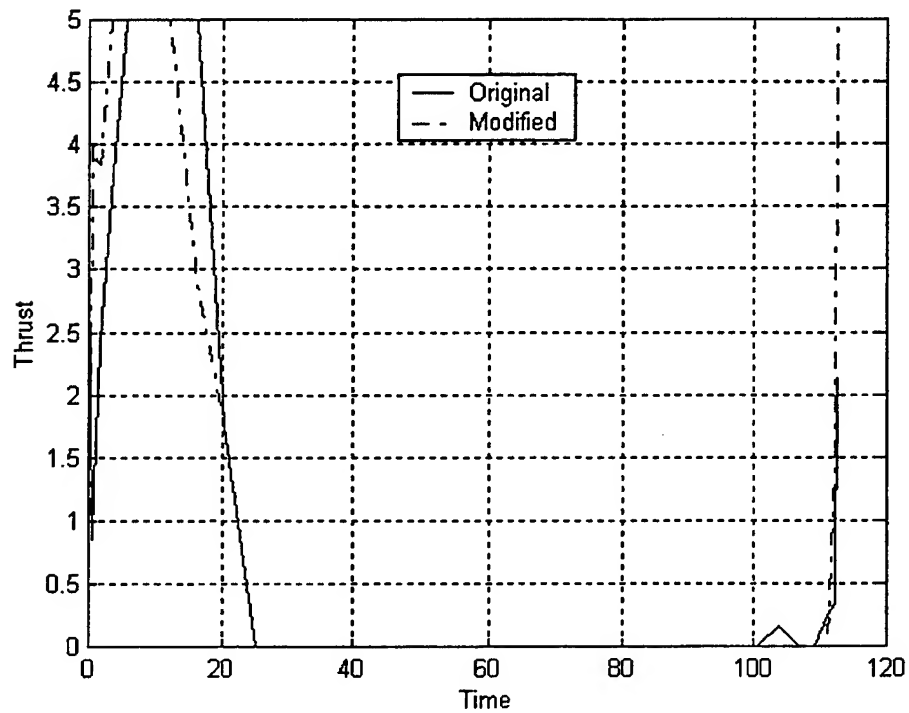


Figure IV-19 Thrust Profile Comparison

The initial large thrusting profiles are similar but shifted. The final thrusting sequence is also different. The final thrust in the modified profile spikes to $T_{\max}=2.1$ vice 5 for the original profile. However, they both appear to be reacting according to the switching function.

The settings of the lower and upper limits also have an effect. In one case, the lower and upper limits of the radius and velocity were changed to reduce the range of values to more physically realistic limits as shown below.

Lower limits: r: ones(n,1)	(r(t=0)=1, all others ≥ 1)
v: 1;.5*ones(n-1,1)	(v(t=0)=1, all others ≥ 0.5)
Upper limits: r: 1;1.5*ones(n-1,1)	(r(t=0)=1, all others ≤ 1.5)
v: ones(n,1)	(v(t=0)=1, all others ≤ 1)

While these limits appeared to make physical sense and agreed with the previous outputs, they effected the results and resulted in costs and solutions similar to the "modified" formulation described above.

2. Stability of Solutions

The stability of the solutions was checked in two ways. First, the outputs of the $n=30$, $t_f=112.6$ were used as the initial guess for another run. If a solution is indeed the optimal solution, then, when used as the initial guess, the output should be the same as the guess. In this case, good stability was demonstrated by the return of a nearly identical solution.

The program was also run using a slightly modified initial guess. The different initial guess consisted of guessing $r_0 = \text{ones}(n,1)$ instead of using the radius results of a previous run. The results also compared well against the previous run.

3. Effect of Increasing the Number of LGL Points

The number of LGL points effected the solutions and sometimes did not yield any solution. For example, the case of $t_f = 112.6$ was run with numerous different numbers of LGL points. The results presented earlier resulted from $n=30$. Runs of $n=40$ and $n=50$ were also performed. The radius and thrust profiles of each ($n=30, 40, 50$) are presented in Figure IV-20. The $n=40$ radius profile is similar to $n=30$ but the thrust profile shows a notch near $t=10$ and an additional thrust spike near $t=105$. The cost was 0.78106 which is 0.44 percent less than for $n=30$. The $n=50$ run yielded poor state and control profiles. Numerous runs were done using different initial guesses but the results always showed the choppiness seen in Figure IV-20. The cost was 0.77395 which is 1.3 percent less than for $n=30$.

A similar problem occurred for cases of $t_f = 80$. The radius and thrust profiles for cases of $n=25, n=35$, and $n=45$ are presented in Figure IV-21. As the number of LGL points increases the radius and thrust profiles become worse. The radius profile has discontinuities and the thrust profile becomes more erratic.

The number of points also greatly affected the solution time. This analysis was conducted on a Sun Sparc 10 workstation using MATLAB 5.2 and NPSOL. Typical run times were 30 minutes for $n=20$, 1.5 hours for $n=30$, 3 hours for $n=40$, and 5 hours for $n=50$.

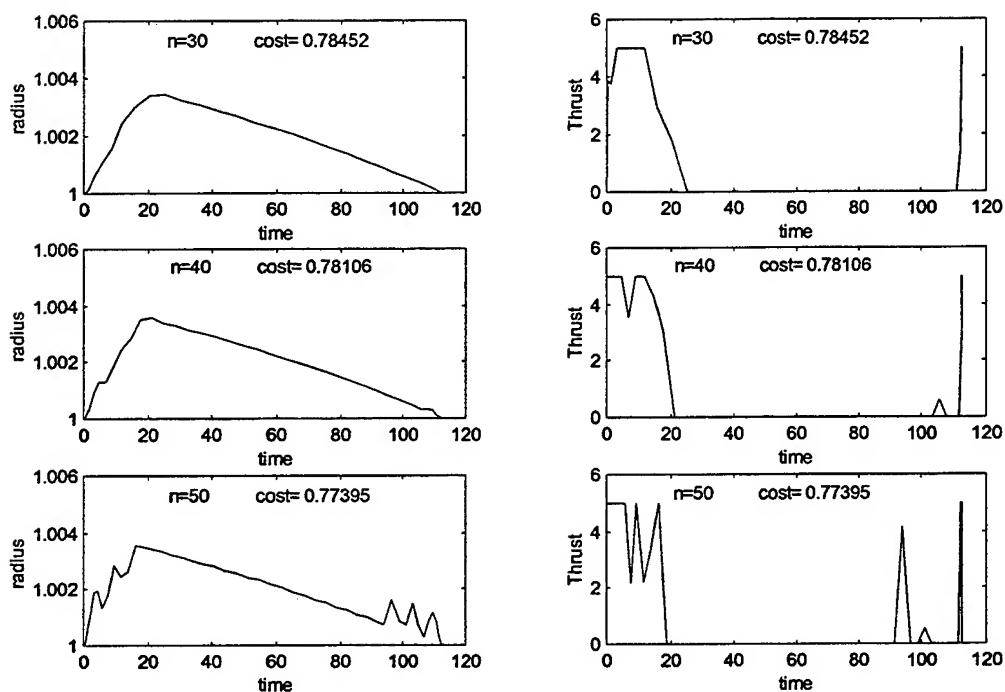


Figure IV-20 Variations of $t_f=112.6$ Runs with Number of LGL Points

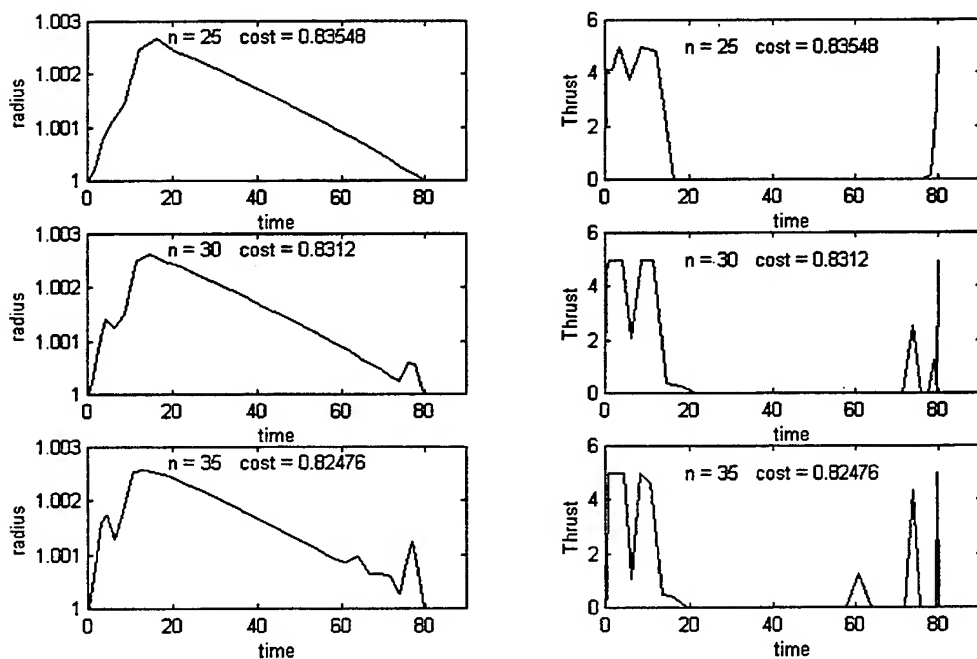


Figure IV-21 Variations of $t_f=80$ Runs with Number of LGL Points

THIS PAGE INTENTIONALLY LEFT BLANK

V. ANALYSIS BY AN INDIRECT METHOD

Indirect methods of optimization rely on the necessary optimality conditions derived from the minimum principle. These necessary conditions are solved for the optimal trajectory by solving a nonlinear two point boundary value problem to obtain the Lagrange multipliers and costates. [Ref. 11] There are several difficulties with indirect methods. Firstly, the method requires that the necessary conditions be derived analytically. Secondly, the indirect methods require a very good initial guess [Ref. 9].

The output of the direct method, including the costates estimates, are used as the initial guess for a multiple shooting algorithm developed at NPS. This code contains three primary steps. First, it loads the states and costates from a data file for use as the initial guess. This data file was either the output obtained from the direct method or the output from a previous run with this software. The software then sets up the initial Jacobian matrix. Lastly, it uses a quasi-Newtonian iteration to get the solution to the two point boundary value problem (TPBVP). The user controls the iteration accuracy requirement and, more importantly, the number of iterations. The number of iterations must be large enough to reach convergence.

Unfortunately, a converged solution was not obtained. The indirect method is extremely sensitive to the initial guess. Both the filtered and the original "noisy" costate estimates obtained from the direct method were used as the initial guesses. Neither resulted in a converged solution and both are probably too poor for convergence.

Alternatively, there might be errors in coding as no analysis was done to validate the process. Attempts with slightly modified costates improved convergence, but still did not provide a converged solution. Therefore, this chapter presents the method of analysis and shows the “best” solution obtained using the original "noisy" costates. These results are neither optimal nor feasible and, therefore, should not be compared against the results of the direct analysis.

The states and costates for the initial guess are loaded from the data file, but not the controls. The controls must be obtained in terms of the states and costates. Figure V-1 contains the code that calculated the thrust angle, ϵ , and thrust magnitude, T , based on given states and costates.

```

eps=atan(lamdg/(v*lamdv));
Switch=1/Tf+lamdv*cos(eps)/(ma*B)+lamdg*sin(eps)/(ma*v*B)-lamdm/(Ve*B);

if Switch>=0
    T=0;
elseif Switch<0
    T=Tmax;
end

```

Figure V-1 Thrust and Thrust Angle Equations

These equations are based upon the optimality condition and switching function developed in Chapter IV and repeated here.

$$\frac{\partial H}{\partial \epsilon} = -\lambda_v \frac{T \sin \epsilon}{mB} + \lambda_\gamma \frac{T \cos \epsilon}{mvB} = 0 \quad (\text{IV-6})$$

$$S = \frac{1}{t_f} + \lambda_v \frac{\cos \epsilon}{mB} + \lambda_\gamma \frac{\sin \epsilon}{mvB} - \lambda_m \left(\frac{1}{v_e B} \right) \quad (\text{IV-7})$$

For bang-bang control, the thrust is a maximum when the switching function is less than zero and a minimum when greater than zero. The switching function is discussed further in the Chapter VI.

Converged solutions were not obtained. Convergence was measured by the Euclidean norm of the difference between consecutive solutions during the iteration process. A converged solution returns a value of approximately 10^{-5} to 10^{-6} . Values on the order of 10^{-2} were obtained. The non-convergence is measurable by the norm and visible in the states and costates.

The current non-converged results are presented for the fixed final time case of $t_f = 112.6$. Figures V-2 and V-3 provide the best solutions obtained with a convergence measure of approximately 5.75×10^{-2} . The states have an oscillatory motion. This oscillation decreases in amplitude as the convergence measure decreases.

The costates of periodic states must also be periodic. Periodic states or costates were not obtained. The costates of states without a final time constraint should be zero (see Equation IV-19). In Figure V-3, the theta costate meets this requirement. The mass costate is close to zero but the other costates are not periodic. Note that, since a converged solution was not obtained, these comparisons against theory are simply to illustrate how non-optimal solutions may be detected visually from the costate plots.

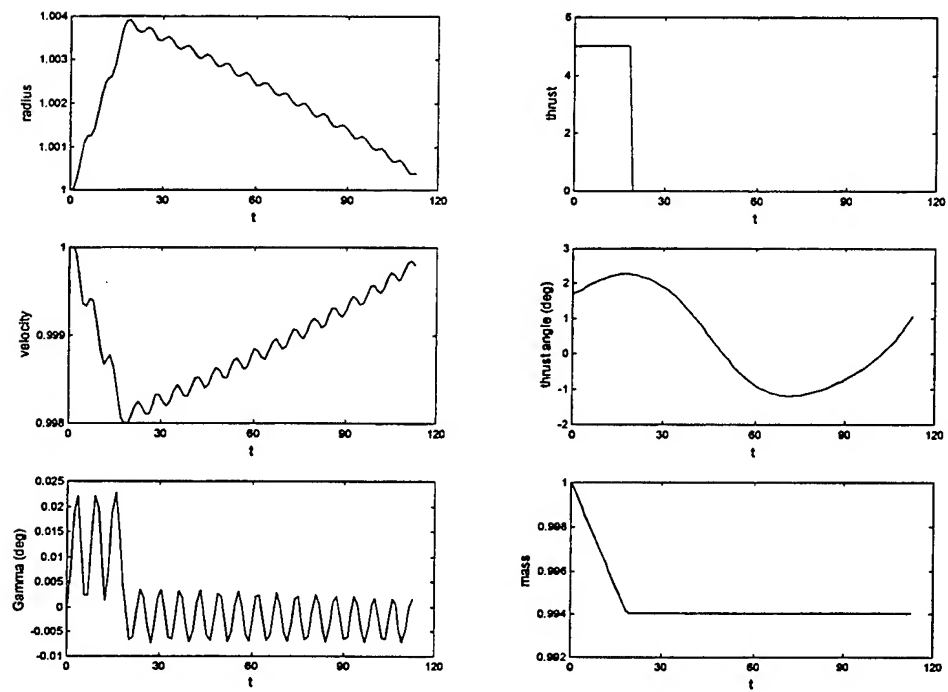


Figure V-2 Non-Convergent States and Controls, Convergent Measure = 0.0575

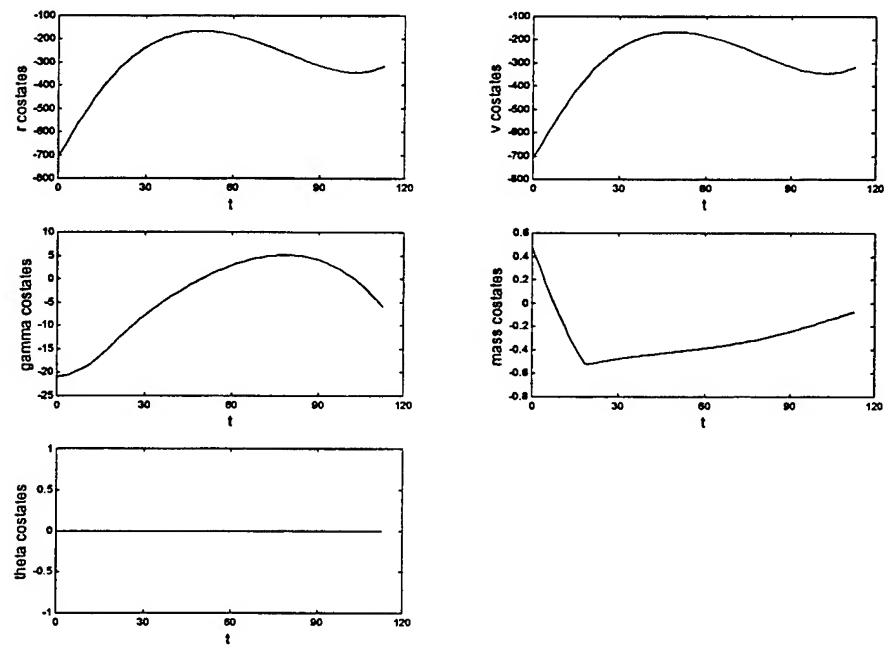


Figure V-3 Non-Convergent Costates, Convergent Measure = 0.0575

As stated earlier, the indirect solutions rely upon the optimality conditions. These conditions were checked against the results provided above. Figure V-4 provides the plot of the optimality condition on ϵ , $\frac{\partial H}{\partial \epsilon} = 0$. The optimality condition appears to be met. This is surprising since the plot is based upon data from a non-convergent result.

The indirect method was very sensitive to the initial guess and the number of iterations was also critical. Obviously, the number of iterations must be enough to reach convergence. Low number of iterations may lead to wildly varying results. The estimate of the optimal solution from the direct method allowed these results to be easily discounted. Figure V-5 provides examples of the results obtained from very low numbers of iterations. Run times were approximately one to three minutes per iteration on a Pentium II at 200 MHz.

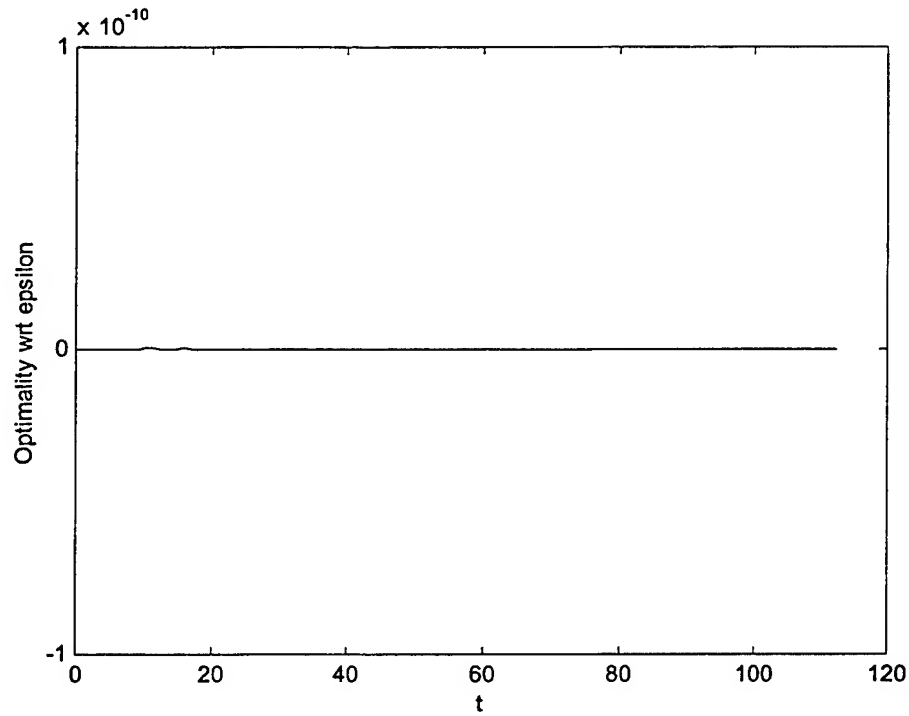


Figure V-4 Plot of Optimality Condition, $\frac{\partial H}{\partial \epsilon}$

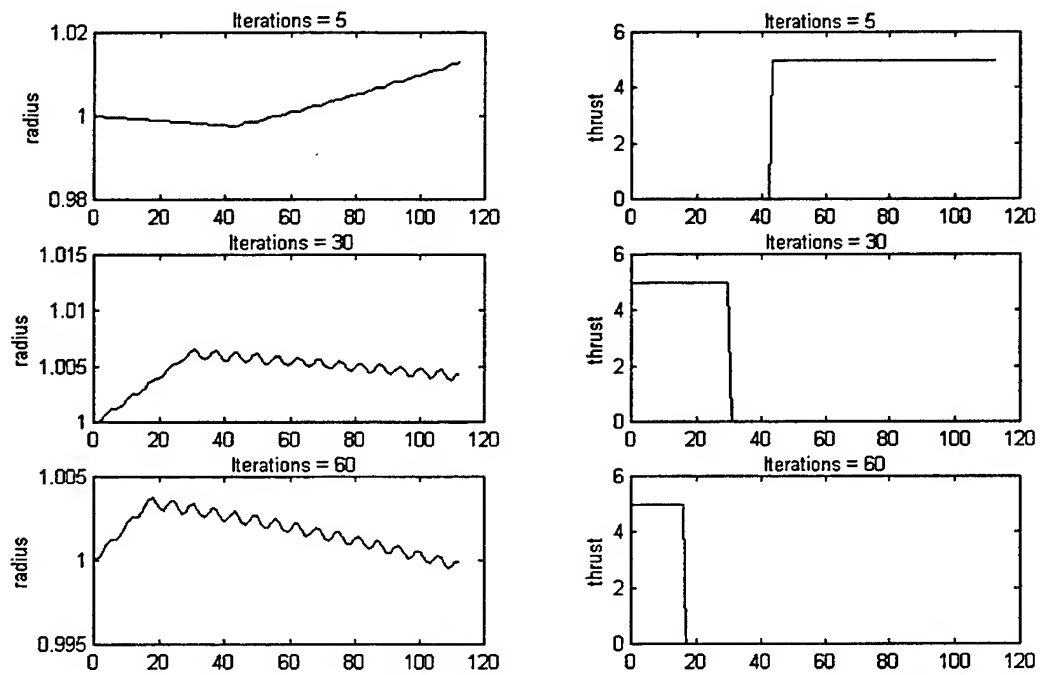


Figure V-5 Indirect Method Responses to Fixed Number of Iterations

VI. ANALYSIS OF THE SWITCHING STRUCTURE

Analysis of the switching function and the effect of varying the thrust control authority provided interesting results related to singular thrust arcs. [Ref. 2] Singular thrust arcs result when the switching function remains at zero instead of simply crossing it (i.e., switching). This was observed in the thrust profiles and switching functions obtained from the direct method.

The effect of increasing levels of thrust was studied using DIDO. It was suspected that a maximum thrust limit for bang-bang control existed. [Ref. 3] Figure VI-1 contains the thrust plots resulting from four different thrust levels (5, 15, 50, 100) for a fixed final time of 700 and $n=50$ LGL points. The cases of $T_{\max} = 5$ and $T_{\max} = 15$ both reach their maximum thrust levels. The cases of $T_{\max} = 50$ and $T_{\max} = 100$ each peak at a thrust level of approximately 34.5.

Thrusting of this type is predicted based upon the totality of extremal thrust-arcs described by: [Ref. 2]

$$T = \begin{cases} 0 & S < 0 \\ T_s & \text{whenever } S \equiv 0 \\ T_{\max} & S > 0 \end{cases} \quad (\text{VI-1})$$

where S is the switching function and T_s is the singular thrust. This highlighted the need to further analyze the switching function. The values of the switching function and the thrust profiles are plotted for each of the cases in Figures VI-2 through VI-5. Included on the plots are the relevant values of n , time, S , and thrust.

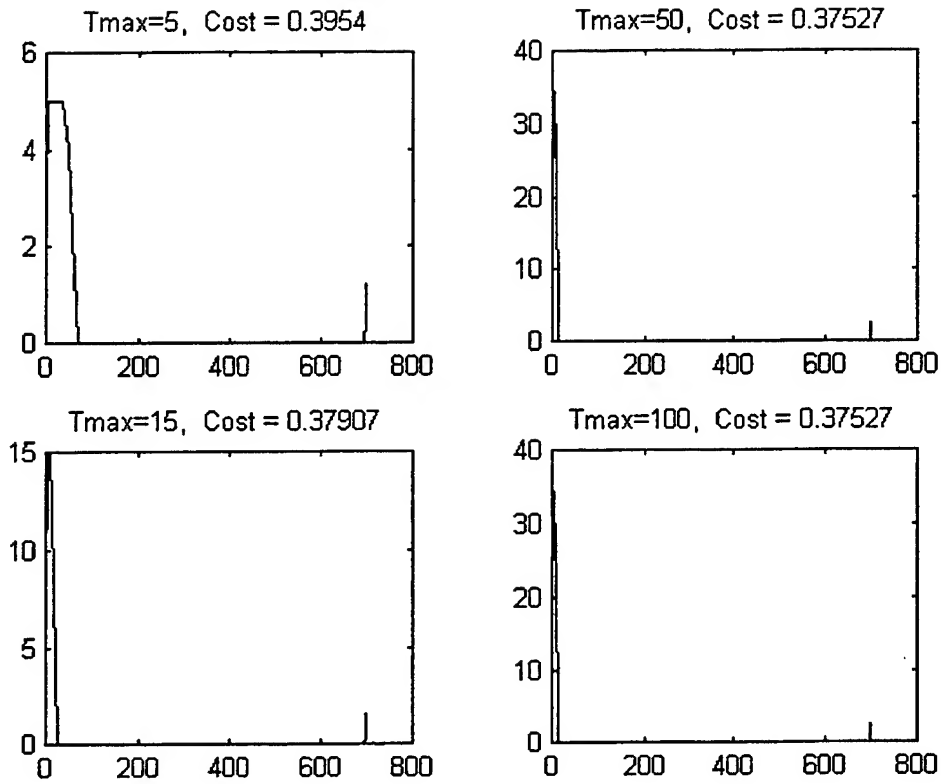


Figure VI-1 Thrust Profiles for Increasing T_{\max} at final time of 700

Figures VI-2 and VI-3 contain the thrust profiles and switching function of the $T_{\max} = 5$ and $T_{\max} = 15$ cases, respectively. In these cases, both have periods during which the switching function is approximately zero at which time the thrust is neither T_{\max} nor zero, but at some varying singular thrust level, T_s . The singular thrusting occurs when the magnitude of the switching function is less than 10^{-6} .

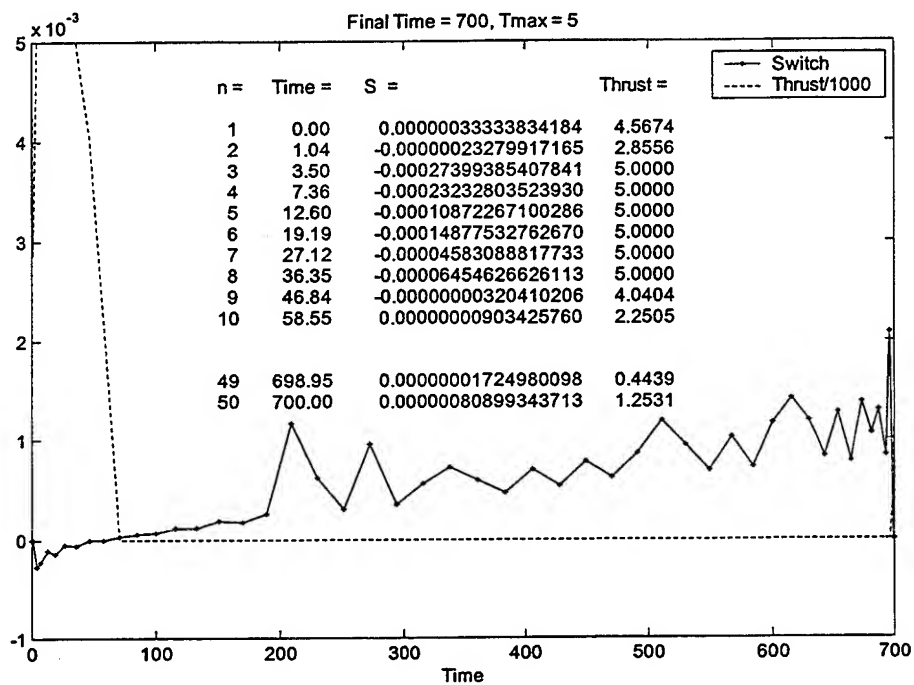


Figure VI-2 Switching and Thrust for $T_{\max} = 5$ and $t_f = 700$

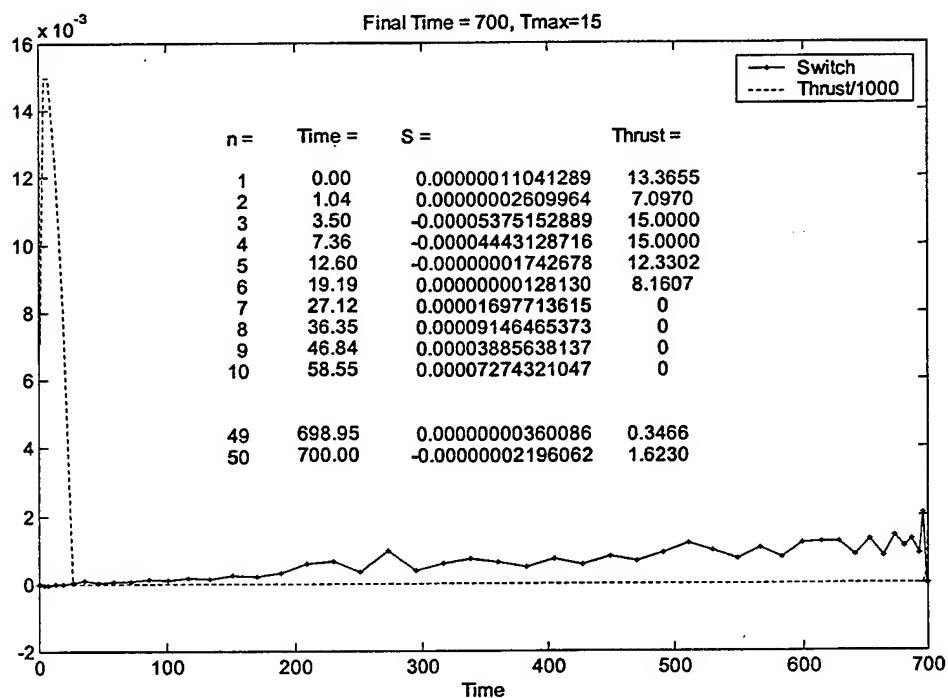


Figure VI-3 Switching and Thrust for $T_{\max} = 15$ and $t_f = 700$

The cases of $T_{\max} = 50$ and $T_{\max} = 100$, shown in Figures VI-4 and VI-5, are different. Each case experiences a period in which the switching function is equal to zero. The thrust level varies during this period and at no time does it reach T_{\max} . Though it appears to spike similar to a bang-bang type profile, it is not bang-bang. This is a different thrust regime known as singular thrust-arcs. [Ref. 2]. Values of interest are included on the plots.

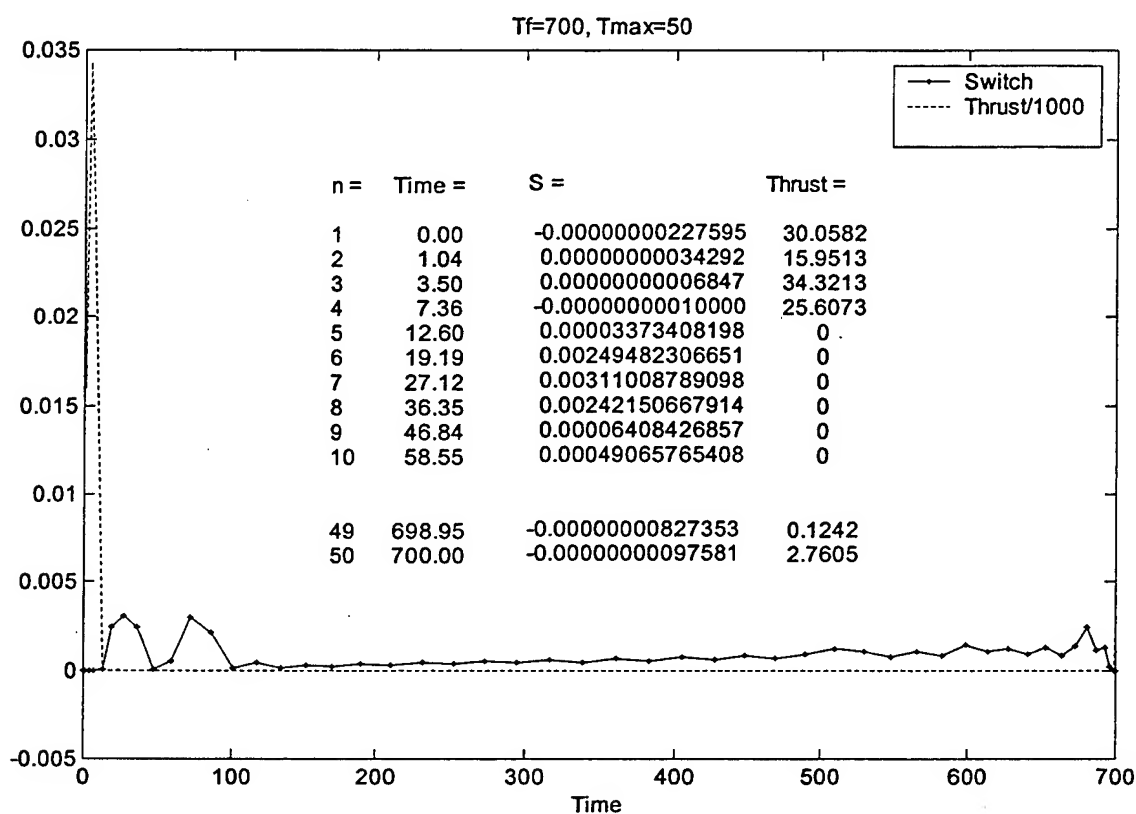


Figure VI-4 Switching and Thrust for $T_{\max} = 50$ and $t_f = 700$

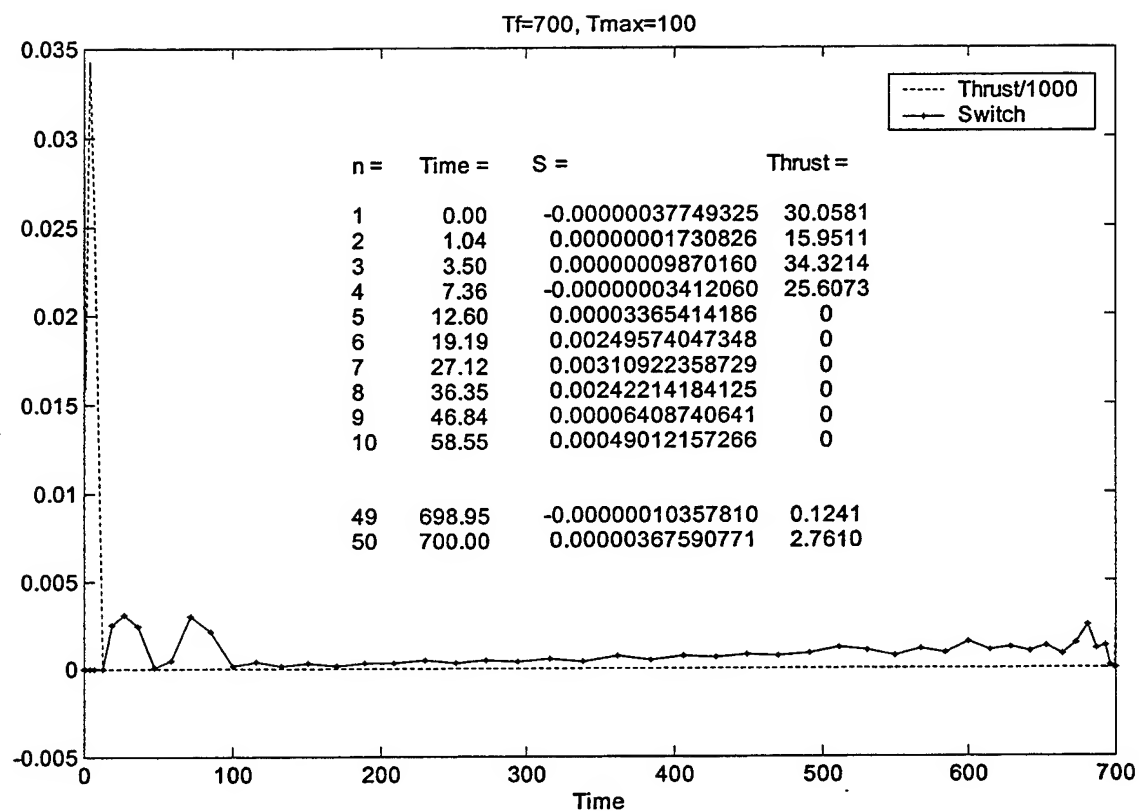


Figure VI-5 Switching and Thrust for $T_{\max} = 100$ and $t_f = 700$

THIS PAGE INTENTIONALLY LEFT BLANK

VII. CONCLUSIONS

The direct Legendre pseudospectral method provides solutions for the periodic orbital maintenance problem that appear to be more efficient than a Hohmann transfer. Numerical analysis indicates savings of 1 to 5 percent over an impulsive Hohmann transfer. Savings increase when compared to a finite-burn Hohmann transfer by as much as 6 percent [Ref. 3]. Further analysis into the cost ratio of the periodic control to the mid-FKT is needed to obtain the true form of the cost plot (see Figure IV-6).

The costate estimates resulting from the direct method were apparently noisy, particularly near the beginning and ending times of the period. The "noise" was filtered and the resultant costates compared against the optimization theory. The costates did not violate the optimization theory as demonstrated in Chapter IV.

The costate estimates are apparently unreliable for this problem. This is curious as costate estimates for the orbit transfer problem [Ref. 4] have been obtained from NPSOL. As discussed in Chapter IV, the solutions are sensitive to the implementation of the problem.

Analysis by the indirect method was also attempted but without success. Convergence of the indirect solution is difficult to obtain due to the sensitivity to the initial guess. The unsmooth costates obtained from the direct method solutions may be partially responsible for limiting convergence.

The thrust profiles were bang-bang with periods of thrust modulation. These thrust-modulated arcs appear to be singular since the switching function was equal to zero. Singular thrust arcs may be particularly beneficial to large flexible structures as thrust modulation will probably excite fewer high frequency vibrations than a bang-bang controller. This has potential benefits to spacecraft payloads, structures, experiments, and inhabitants.

More work in this area is certainly needed. The optimal control problem is still not fully solved, but the solution presented here appears to provide advantages to mission planners. Employing the optimal orbit maintenance technique along with properly sized thrusters can significantly increase mission duration and reduce cost.

LIST OF REFERENCES

1. Ross, I. M., and Alfrend, K. T., "Low-Earth-Orbit Maintenance: Reboost vs Thrust- Drag Cancellation," *Journal of Guidance, Control, and Dynamics*, Vol. 18, No. 4, Nov. 1994, pp. 930-932.
2. Ross, I.M., "An Analysis of First-Order Singular Thrust-Arcs in Rocket Trajectory Optimization," *Acta Astronautica, Journal of the International Academy of Astronautics*, Vol. 39, No. 6, 1996, pp. 417-422.
3. Jensen, K.E., *Fuel-Optimal Low-Earth-Orbit Maintenance*, Master's Thesis, Naval Postgraduate School, Monterey, California, June 1997.
4. Fahroo, F., and Ross, I.M., "Costate Estimation by a Legendre Pseudospectral Method," *Proceedings of the 1998 AIAA GNC Conference*, Boston, Massachusetts, August 1998, AIAA Paper 98-4222.
5. Vallado, D.A., *Fundamentals of Astrodynamics and Applications*, McGraw-Hill Companies, Inc, New York, New York, 1997.
6. Bryson, A.E., Jr, and Ho, Yu-Chi, *Applied Optimal Control: Optimization, Estimation, and Control*, John Wiley & Sons, New York, New York, 1975.
7. Ross, I.M., Class notes for AA 4850, Spacecraft Optimization and Control, Naval Postgraduate School, Monterey, California, 1999.
8. Kirk, D.E., *Optimal Control Theory, An Introduction*, Prentice-Hall, Englewood Cliffs, New Jersey
9. Hall, A.O., *A MATLAB GUI for a Legendre Pseudospectral Algorithm for Optimal Control Problems*, Master's Thesis, Naval Postgraduate School, Monterey, California, June 1999.
10. Gill, P.E., et al, Technical Report SOL 86-1, *User's Guide for NPSOL 5.0: A FORTRAN Package for Nonlinear Programming*, Department of Mathematics, University of California, San Diego, California, Revised July 30, 1998.
11. Betts, J.T., "Survey of Numerical Methods for Trajectory Optimization," *Journal of Guidance, Control, and Dynamics*, Vol. 21, No. 2, March-April 1998, pp. 193-207.

THIS PAGE INTENTIONALLY LEFT BLANK

INITIAL DISTRIBUTION LIST

1. Defense Technical Information Center 2
8725 John J. Kingman Rd., Ste 0944
Ft. Belvoir, VA 22060-6218
2. Dudley Knox Library 2
Naval Postgraduate School
411 Dyer Rd.
Monterey, CA 93943-5101
3. Department Chairman, Code AA 1
Department of Aeronautics and Astronautics
Naval Postgraduate School
Monterey, CA 93943-5000
4. Department of Aeronautics and Astronautics 3
ATTN: Professor I. Michael Ross, Code AA/Ro
Naval Postgraduate School
Monterey, CA 93943-5000
5. Space Systems Academic Group 1
Chairman, Code SP
Naval Postgraduate School
Monterey, Ca 93943-5000
6. Department of Mathematics 1
ATTN: Professor Fariba Fahroo, Code Ma/Ff
Naval Postgraduate School
Monterey, CA 93943-5000
7. Major Lawrence Halbach 5
14885 Greenhill Crossing Dr
Haymarket, VA 20169